



















The dark side of early galaxies: GEKO uncovers dark-matter fractions at $z \sim 4 - 6$

A. Lola Danhaive ^{1,2*}, Sandro Tacchella ^{1,2}, Andrew J. Bunker ³, Emma Curtis-Lake ⁴, Anna de Graaff ⁵, Francesco D'Eugenio ^{1,2}, Qiao Duan ^{1,2}, Eiichi Egami ⁶, Daniel J. Eisenstein ⁷, Benjamin D. Johnson ⁷, Roberto Maiolino ^{1,2}, William McClymont ^{1,2}, Marcia Rieke ⁶, Brant Robertson ⁸, Fengwu Sun ⁷, Christopher N. A. Willmer ⁶, Zihao Wu ⁷, Yongda Zhu ⁶

¹Kavli Institute for Cosmology, University of Cambridge, Madingley Road, Cambridge, CB3 0HA, UK

²Cavendish Laboratory, University of Cambridge, 19 JJ Thomson Avenue, Cambridge, CB3 0HE, UK

³Department of Physics, University of Oxford, Denys Wilkinson Building, Keble Road, Oxford OX1 3RH, UK

⁴Centre for Astrophysics Research, Department of Physics, Astronomy and Mathematics, University of Hertfordshire, Hatfield AL10 9AB, UK

⁵Max-Planck-Institut für Astronomie, Königstuhl 17, D-69117, Heidelberg, Germany

⁶Steward Observatory, University of Arizona, 933 N. Cherry Avenue, Tucson, AZ 85721, USA

⁷Center for Astrophysics | Harvard & Smithsonian, 60 Garden St., Cambridge MA 02138 USA

⁸Department of Astronomy and Astrophysics, University of California, Santa Cruz, 1156 High Street, Santa Cruz, CA 95064, USA

Accepted XXX. Received YYY; in original form ZZZ

ABSTRACT

JWST/NIRCam slitless spectroscopy enables dynamical mass measurements for typical star-forming galaxies only a billion years after the Big Bang. We model the H α morpho-kinematics of 163 galaxies at redshift $z \approx 4-6$ from FRESCO and CONGRESS (with JADES imaging), using the geko code, and infer rotational velocities and dispersions within r_e . Our sample spans $\log M_\star \approx 7-10$ and $\log M_{\text{dyn}} \approx 9-11$. Gas masses are estimated via scaling relations, yielding baryonic masses and dark-matter (DM) fractions $f_{\text{DM}}(r < r_e)$ within the H α half-light radius. We find high median fractions of $\langle f_{\text{gas}} \rangle = 0.77$ and $\langle f_{\text{DM}} \rangle = 0.73$, where f_{gas} is measured with respect to the baryonic mass and f_{DM} with respect to the DM+baryonic mass. About two-thirds of systems are DM-dominated within $r_e \sim 0.5 - 1$ kpc. Both f_{gas} and f_{DM} decrease with stellar mass, **consistent with simulations**. The stellar Tully-Fisher relation shows a tentative offset to higher v_{circ} at fixed M_\star and substantial intrinsic scatter, suggesting that the relation is only beginning to emerge at $z \sim 5$. We measure a negative correlation between f_{DM} and baryonic surface density Σ_{bar} , weaker but broadly consistent with trends at cosmic noon and at $z \sim 0$. Qualitatively comparing with modified NFW profiles coupled to an empirical stellar-to-halo mass relation suggests that the lowest $f_{\text{DM}} (\lesssim 0.4)$ **require cored inner DM profiles**, while the highest fractions favour cuspier profiles, potentially reflecting adiabatic contraction. Overall, the elevated f_{gas} and f_{DM} at $z \gtrsim 4$ are compatible with progenitors of baryon-dominated systems at $z \sim 2$ and naturally anticipate overmassive black holes at fixed M_\star .

Key words: galaxies: kinematics and dynamics – galaxies: evolution – galaxies: high-redshift – galaxies: structure – DM

1 INTRODUCTION

The nature and physics of dark matter (DM) is to this day one of the biggest outstanding questions in astrophysics. In the widely adopted standard cosmological model of Λ CDM, DM haloes form from the collapse of overdensities in the early Universe, allowing baryons to accrete, cool, and form stars. This process is the basis of galaxy formation, and predicts the hierarchical growth of galaxies. However, the physics and interplay between the baryons and the DM remain remarkably poorly constrained.

In fact, measuring the DM mass content of galaxies and their haloes observationally is a challenge, as often even the full baryonic

mass is difficult to constrain. Many approaches have been adopted to indirectly constrain the galaxy-halo connection, such as abundance matching (Marinoni & Hudson 2002; Kravtsov et al. 2004; Conroy et al. 2006; Vale & Ostriker 2006; Tasitsiomi 2007) and clustering analyses (Peacock & Smith 2000; Cooray & Sheth 2002; Smith et al. 2003; Paquereau et al. 2025) based on N-body simulations. Many numerical simulations have measured the stellar-to-halo mass (SMHM) relation and its evolution with redshift (Behroozi et al. 2010; Moster et al. 2010; Rodríguez-Puebla et al. 2017; Behroozi et al. 2019; Tacchella et al. 2018), although its overall normalisation and turnover mass are still debated and model-dependent. In part, this is due to the circularity of modelling inputs and outputs, as cosmological hydrodynamical simulations are usually calibrated to SMHM relations measured from abundance matching or derived from semi-

* ald66@cam.ac.uk

empirical models. Placing direct observational constraints on this relation would offer important insight on the integrated strength of various fundamental mechanisms which govern the evolution of galaxies, such as stellar feedback, black hole activity, and mergers.

One of the most robust ways of constraining the DM content within galaxies is through the measurement of galaxy kinematics. The rotation curves and pressure support of galaxies reflect their total density profile, providing an estimate of the DM content assuming that the baryonic content is known (Rubin et al. 1980; Burkert 1995; Burkert & Silk 1997; Persic et al. 1996; McMillan 2017; Zhu et al. 2023). The fraction of DM to the total mass, f_{DM} , is a by-product of the mass assembly history of galaxies and of their current growth (see Wechsler & Tinker 2018, and references therein).

The study of these density profiles within dwarf galaxies, defined as having masses of $M_{\star} < 3 \times 10^9 M_{\odot}$, has proved particularly fruitful, revealing a discrepancy between Λ CDM-predicted and observed density profiles known as the core-cusp problem. Where collisionless (cold) DM-only cosmological simulations predict cuspy profiles, with densities increasing steeply at small radii, measurements of the rotation curves in dwarf galaxies in the local Universe show "core"-like profiles that flatten at central radii (Moore 1994; Burkert 1995). This core-cusp problem posed a direct challenge to Λ CDM, with propositions of different types of DM surfacing (Hu et al. 2000; Spergel & Steinhardt 2000). However, many studies have now shown that this problem can be alleviated by invoking strong baryonic feedback, likely from supernovae. This feedback, especially through repeated bursts of star formation, can flatten the DM cusp into a core (Read & Gilmore 2005; Pontzen & Governato 2012, 2014; Martizzi et al. 2013). This process has been observed in hydrodynamical simulations (e.g., Chan et al. 2015; Read et al. 2016, and references therein), but details such as mass, redshift, and environmental dependence remain uncertain. Interestingly, cases of profiles cuspiest than Λ CDM profiles have also been found (Sonnenfeld et al. 2012; Wang et al. 2020; Li et al. 2022), which could be caused by adiabatic contraction of the DM halo due to high baryonic densities in the galaxy core (Blumenthal et al. 1986; Gnedin et al. 2004; Li et al. 2022).

Another important relation that relates the potential of the DM halo to its host galaxy is the observed tight relation between stellar (or baryonic) mass and circular velocity, named the stellar (or baryonic) Tully-Fisher relation (TFR; Tully & Fisher 1977). The baryonic mass TFR (bTFR) is the more fundamental of the two, as it holds even down to low masses (McGaugh et al. 2000; McGaugh 2005). Both TFRs have been found to hold for star-forming galaxies from $z \approx 0$ (Reyes et al. 2011; Lelli et al. 2016) to cosmic noon (Miller et al. 2011; Übler et al. 2017), albeit with an increase of scatter and a decrease of zero-point offset with redshift. Measuring the position of galaxies on the TFR plane at $z > 4$ can provide constraints on the properties of the underlying haloes and their relative contribution to the total mass of the galaxy.

The detailed mapping of rotation curves of galaxies in the local Universe has revealed that $\log(M_{\star} [M_{\odot}]) = 10 - 11$ star-forming galaxies are baryon-dominated in their central ~ 1 kpc, but DM dominated within their half-light, or effective, radii r_e (Rubin et al. 1985; Martinsson et al. 2013). On the other hand, early-type galaxies (ETGs) at $z \sim 0$ are heavily baryon-dominated within r_e , suggesting a diverging mass assembly history (Noordermeer et al. 2007; Cappellari et al. 2013a; Serra et al. 2016). Interestingly, studies of DM fractions at cosmic noon ($z \approx 2$) in $\log(M_{\star} [M_{\odot}]) \gtrsim 9.5$ galaxies found them to be similar to local ETGs, with baryon-dominated cores (Price et al. 2016; Wuyts et al. 2016; Genzel et al. 2017, 2020; Nestor Shachar et al. 2023). Genzel et al. (2020) interpret these findings as

evidence for cored DM profiles, motivated by the rapid formation of massive haloes and galaxies at $z \sim 1 - 3$. In fact, cosmic noon marks the peak of the cosmic star-formation rate (SFR) density (Madau & Dickinson 2014), where gas accretion rates reached peak values (Tacconi et al. 2020) and stellar mass doubling scales were on the order of $t < 0.4$ Gyr.

Measurement of the DM content of high-redshift galaxies ($z \geq 4$) was made possible with the advent of the *James Webb Space Telescope* (*JWST*), whose NIRCam and NIRSpec instruments probe ionised gas emission lines out to $z \sim 10$. While kinematic studies had previously been done at such early times through cold gas measurements (i.e. [C II] or CO) from ground based telescopes such as the Atacama Large Millimeter Array (ALMA, e.g., Lelli et al. 2021; Rizzo et al. 2020, 2021; Roman-Oliveira et al. 2023; Pope et al. 2023; Rowland et al. 2024), the lack of constraints on the stellar mass made estimating f_{DM} difficult. Using kinematic modelling of *JWST*/NIRSpec Multi Shutter Array (MSA) data (see also Saldana-Lopez et al. 2025), de Graaff et al. (2024a,b) found that the five low-mass $\log(M_{\star} [M_{\odot}]) < 9$ galaxies in their $z \sim 6 - 8$ sample were DM dominated within r_e ($f_{\text{DM}} \sim 0.7$). By studying similar galaxies in the TNG50 simulations (Pillepich et al. 2019), de Graaff et al. (2024b) suggest that DM-dominated $\log(M_{\star} [M_{\odot}]) = 8 - 9$ galaxies at $z \sim 6$ are the progenitors of massive baryon-dominated systems at $z \sim 2$. This finding predicts a DM dominated phase of early galaxy formation, with expectations that all low-mass galaxies have low baryon fractions in their central region.

When studying the DM fractions in the central regions of galaxies, it is also important to consider the effects of black holes (BHs) which could be hosted in their cores. Although BHs have been shown to have masses which are only a small fraction of the total dynamical mass (Kormendy & Ho 2013), recent *JWST* studies have uncovered "overmassive" BHs in the early Universe, with $M_{\text{BH}}/M_{\star} \sim 0.1 - 0.01$ (Harikane et al. 2023; Kokorev et al. 2023; Übler et al. 2023; Maiolino et al. 2024b; Juodžbalis et al. 2025a; Jones et al. 2025), even reaching $M_{\text{BH}}/M_{\star} > 2$ (Juodžbalis et al. 2025b). If the relatively low-mass galaxies at $z > 4$ host massive black holes which experience accretion phases, then they could play a significant role in the galaxy's mass assembly history. Importantly, active galactic nuclei (AGN)-driven outflows can heavily disrupt the surrounding gas, particularly in low-mass galaxies (Sijacki et al. 2007; Nelson et al. 2019; Koudmani et al. 2021, 2022; Carniani et al. 2024). The presence of such AGNs is important to study as it currently introduces more uncertainties in the interpretation of our kinematic measurements.

With the synergy of NIRCcam imaging and grism data, the kinematics of ~ 200 galaxies at $z = 4 - 6$ were measured in Danhaive et al. (2025a) using a new forward-modelling Bayesian code, the Grism Emission-line Kinematics tOol (Geko, Danhaive & Tacchella 2025)¹. This sample is comprised of $\log(M_{\star} [M_{\odot}]) \approx 7 - 10.5$ star-forming galaxies, with a wide range of rotational support v/σ_0 . As shown in Danhaive et al. (2025a), many of these galaxies have large dynamical masses compared to their stellar masses, pointing to large contributions from gas and DM. In this paper, we study the mass content of these galaxies in detail, placing the first statistical constraints on DM fractions at high redshift $z > 4$. We briefly introduce our sample and methodology in Sec. 2, then present our dynamical mass measurements and discuss in the context of the Tully-Fisher (TFR) relation in Sec. 3. We present our gas and DM fractions in Sec. 4, and compare them to samples at lower redshift. In Sec. 5, we interpret our measurements in the context of the shapes of DM density profiles,

¹ Available at <https://github.com/angelicalola-danhaive/geko>

and explore potential contributions from BHs. Finally, we summarise our results in Sec. 6. Throughout this work, we assume $\Omega_0 = 0.315$ and $H_0 = 67.4 \text{ km s}^{-1} \text{ Mpc}^{-1}$ (Planck Collaboration et al. 2020).

2 OBSERVATIONS, SAMPLE AND METHODOLOGY

In this section, we present the NIRC*am* grism and imaging data used in this work, along with a description of our sample (Sec. 2.1). We also describe the morpho-kinematic modelling of our sample (Sec. 2.2), which is used to measure the rotational velocities and velocity dispersions of our galaxies. This sample, and the associated kinematic measurements, are described in Danhaive et al. (2025a), so we only summarize them here but refer the reader to that work for more details. Finally, in Sec. 2.3, we detail our derivation of the gas and DM fractions for our sample.

2.1 NIRC*am* data and sample selection

The analysis in this work uses both NIRC*am* imaging and grism spectroscopy. The NIRC*am* grism data is obtained from the FRESCO survey (PI: Oesch, PID: 1895; Oesch et al. 2023; Covelo-Paz et al. 2025) in GOODS-S and GOODS-N, and the CONGRESS survey (PIs: Egami & Sun, PID: 3577; Sun et al. in prep) in GOODS-N. These surveys are comprised of grism data (R mode) in the F444W and F356W filters, respectively, probing H α emission at $z = 3.8\text{--}6.5$. The data is reduced following Sun et al. (2023) and Helton et al. (2024) to obtain 2D spectra for each galaxy in the field of view. The 2D spectra are then continuum subtracted following the 2-step iterative technique described in Kashino et al. (2023) to obtain 2D emission line maps for H α .

In the regions of the FRESCO and CONGRESS surveys, there is a wealth of deep imaging data from the JADES survey (Eisenstein et al. 2023; Rieke et al. 2023). Specifically, the JADES survey has imaging in most of the NIRC*am* wide bands, as well as the F335M and F410M medium bands. In addition, the FRESCO survey obtained imaging in the F182M and F210M bands, and CONGRESS in F090W and F115W, complementing the existing JADES imaging data. For certain regions in our sample, we also have additional medium bands F182M, F210M, F430M, F460M, and F480M from the *JWST* Extragalactic Medium Band Survey (JEMS; Williams et al. 2023) in GOODS-S. The full details on the data reduction and generation of the drizzled mosaics and photometric catalogues can be found in Rieke et al. (2023) and Robertson et al. (2024). This large array of photometric bands, in addition to the grism spectroscopic redshifts and emission line fluxes, allows us to fit the SEDs of all galaxies with PROSPECTOR (Johnson et al. 2021; Tacchella et al. 2023; Simmonds et al. 2024, 2025). We obtain measurements of the stellar masses (M_\star), star-formation rates (SFRs), and star formation histories (SFHs) used in this work.

As mentioned above, the parent sample used in this work is described in Danhaive et al. (2025a). This H α emitter sample is built on the photometric redshift estimates from EAZY (Brammer et al. 2008; Hainline et al. 2024), which are then confirmed by Gaussian fitting of the 1D grism spectrum followed by visual inspection (Helton et al. 2024; Lin et al. 2025). We select galaxies with an H α S/N cut of 10 (582 galaxies), from which we select our final sample of 213 galaxies based on additional S/N cuts and position angle (PA) cuts to ensure that galaxies are at an angle with respect to the grism dispersion direction. Specifically, the 213 galaxies are separated into three samples based on the robustness of the kinematic measurements, as described in Danhaive et al. (2025a). In this paper, we only

consider the 163 galaxies from the gold and silver samples, and we exclude the unresolved sample. The latter contains systems with sizes smaller than the full-width half-maximum (FWHM) of the F444W (or F356W) point-spread function (PSF), or with unresolved velocity gradients. However, for simplicity, we do not further distinguish between the gold and silver subsamples in this paper, treating the 163 galaxies together as our full final sample.

2.2 Morpho-kinematic modelling

To obtain measurements of the rotational velocity and velocity dispersion, we use the Bayesian-inference fitting tool GEKO (Danhaive & Tacchella 2025) which forward models the grism data and compares it with the observed 2D spectrum to obtain the posterior distributions of the input morphological and kinematic model parameters.

The H α emission line map is modelled with a Sérsic profile (Sérsic 1968):

$$I(r) = I_e \exp\left(-b_n \left[\left(\frac{r}{r_e}\right)^{1/n} - 1\right]\right), \quad (1)$$

where I_e is the intensity at the effective radius r_e and n is the Sérsic index. We use the near-UV image from JADES, probed by the F150W filter at $\lambda_{\text{rest}} \approx 2000\text{\AA}$, as a prior for the morphology of the H α line. The rest-frame near-UV is chosen because it traces young stars responsible for ionizing the nearby gas and producing the H α emission. To model the F150W images, we use the Bayesian code PYSERVIC (Pasha & Miller 2023), which models the image with a PSF-convolved Sérsic profile. The width of the priors is obtained by doubling the uncertainties obtained from the PYSERVIC modelling.

The H α gas kinematics are modelled with an arctangent velocity curve (Courteau 1997; Miller et al. 2011)

$$V_{\text{rot}}(r_{\text{int}}, r_t, V_a) = \frac{2}{\pi} V_a \arctan \frac{r_{\text{int}}}{r_t}, \quad (2)$$

where V_{rot} is the rotational velocity at a given radius r_{int} in the intrinsic galaxy plane, V_a is the asymptotic value to which the arctangent rotation curve converges to at large radii $r_{\text{int}} \rightarrow \infty$ and r_t is the turn-around radius of the rotation curve. To project this velocity on the observation plane, we need to account for the galaxy's inclination i :

$$V_{\text{obs}}(x, y) = V_{\text{rot}}(r_{\text{int}}, r_t, V_a) \cdot \sin i \cdot \cos \phi_{\text{int}}, \quad (3)$$

where ϕ_{int} is the polar angle coordinate in the galaxy plane. To compute the inclination, we assume an intrinsic axis ratio $q_0 = 0.2$ to account for the thickness of galaxies at high redshift (Wuyts et al. 2016; Genzel et al. 2017; Price et al. 2020; Übler et al. 2024). We adopt a constant velocity dispersion across the galaxy.

The model H α intrinsic map is convolved with the kinematics to form a model 3D cube, which is then convolved with the instrument PSF and line-spread function (LSF). Finally, using the grism dispersion function, the cube is projected onto the observed grism 2D space. The priors for the kinematic parameters are uniform. We place a constraint on the turn-around radius r_t to be smaller than the effective radius r_e (Miller et al. 2011).

2.3 Gas and DM fractions

In order to infer gas masses from our star-formation rates, we use the empirical relations calibrated in Tacconi et al. (2020). We assume here that the gas component is dominated by the molecular phase, whose mass is constrained in these relations. In dense, highly star-forming systems it is expected that the molecular phase dominates

within r_e , and the atomic phase only contributes to a minor degree (e.g. Leroy et al. 2008; Saintonge et al. 2017). The ionised component is small in most systems (e.g. see Kennicutt & Evans 2012, and references therein). Given the small sizes ($r_e \approx 0.5 - 1$ kpc, Danhaive et al. 2025b) and high specific star-formation rates (sSFR, with mass-doubling timescales of $t_{\text{double}} \lesssim 30$ Myr) of the galaxies in our sample, this is a valid assumption.

In these equations, the molecular gas mass is estimated using the sSFR of the system and the integrated depletion timescale for converting the gas into stars. This timescale depends on the redshift and therefore provides a more accurate conversion than fixed redshift relations (e.g. Kennicutt 1998). Furthermore, the latter is calibrated to the local universe, where gas fractions are overall lower, whereas the Tacconi et al. (2020) relations are calibrated from $z \sim 0 - 5.5$ from almost 2000 objects or stacks (see also Saintonge et al. 2017; Tacconi et al. 2018; Freundlich et al. 2019). Specifically, the gas-to-stellar mass ratio $\mu_{\text{gas}} = M_{\text{gas}}/M_{\star}$ scales with redshift z , sSFRs, and stellar mass M_{\star} , where the scaling factors are computed using observational measurements of ionized and molecular gas from the literature. The relation for μ_{gas} is:

$$\begin{aligned} \log \mu_{\text{gas}} = & A + B \times (\log(1+z) - F)^2 \\ & + C \times \log(\text{sSFR}/\text{sSFR}_{\text{MS}}(z, M_{\star})) \\ & + D \times (\log M_{\star} - 10.7), \end{aligned}$$

with the star-forming main sequence (SFMS) defined as in Speagle et al. (2014), and the parameters A, B, C, D and F are the parameters obtained in Tacconi et al. 2020 (Table 2b) from error-weighted, multi-parameter regression. SFMSs such as Speagle et al. (2014) can suffer from sample selection effects, especially on the low mass end, which can bias the inferred relation (e.g. McClymont et al. 2025b; Simmonds et al. 2025). We also note that the Kennicutt (1998) relation assumes solar metallicities, which can have significant impacts (~ 0.3 dex) on the inferred SFRs, particularly for low-mass, metal-poor galaxies.

Using the aforementioned scaling relation, we can then calculate gas fractions on the galaxy scale,

$$f_{\text{gas}} = \frac{\mu_{\text{gas}}}{1 + \mu_{\text{gas}}} = \frac{M_{\text{gas}}}{M_{\text{gas}} + M_{\star}}, \quad (4)$$

and infer the total baryonic masses:

$$M_{\text{bar}} = M_{\text{gas}} + M_{\star} = (\mu_{\text{gas}} + 1)M_{\star}. \quad (5)$$

To quantify the uncertainties in our inferred gas fractions, we propagate the uncertainties from the inputs to the scaling relation (M_{\star} and SFR), along with the uncertainties of the constant parameters of the relation itself (A, B, C, D and F). To assess the systematics introduced by our choice of gas mass estimate, we compare the f_{gas} measurements obtained from the scaling relation to those inferred by a simple conversion

$$M_{\text{gas}} = \text{SFR} \times t_{\text{dep}} \quad (6)$$

with a depletion time $t_{\text{dep}} = 0.5 - 1$ Gyr. Although using this relation increases the intrinsic scatter, our median fractions remain consistent. If instead we change the SFMS used in the Tacconi et al. (2020) relation, from Speagle et al. (2014), and adopt the one from Simmonds et al. (2025), we find that our inferred gas fractions are on average higher by $\Delta f_{\text{gas}} \approx 0.05 - 0.1$. We note that in both of these cases, the change in f_{gas} does not visibly affect the median values of our inferred dark-matter fractions. However, it is important to note these uncertainties in the gas fractions, which can only be addressed with constraints from direct observations of the molecular gas content.

In virial equilibrium, the circular velocity of galaxies at a radius r can be related to the combined effects of gravity and turbulence-induced pressure. The former is reflected in the rotational velocity, and the latter is an asymmetric drift correction to account for the pressure support (Burkert et al. 2010; Newman et al. 2013; Wuyts et al. 2016). For an exponential disk, the circular velocity can be written as:

$$v_{\text{circ}}(r) = \sqrt{v_{\text{rot}}^2(r) + 2(r/r_s)\sigma_0^2}. \quad (7)$$

The circular velocity reflects the gravitational potential of the galaxy and is hence directly related to the dynamical mass,

$$M_{\text{dyn}} = k_{\text{tot}} \frac{r_e v_{\text{circ}}^2(r_e)}{G}, \quad (8)$$

where G is the gravitational constant and k_{tot} is the virial coefficient (Price et al. 2020). The virial coefficient k_{tot} allows us to infer the total dynamical masses based on measurements out to r_e . If we instead compute v_{circ} using a generalised Sérsic profile (rather than an exponential disk, $n = 1$), our inferred dynamical masses remain consistent within $\Delta(\log M_{\text{dyn}}) \lesssim 0.07$ (with median $\Delta(\log M_{\text{dyn}}) \lesssim 0.02$). We present results for the exponential disk assumption to provide a more direct comparison to other works in the literature. Because we have modelled our galaxies with $q_0 = 0.2$, we choose $k_{\text{tot}} = 1.8$ as it is the coefficient for galaxies with $q_0 = 0.2$ and $n \sim 1 - 4$ (Price et al. 2022). We note that varying q_0 in the interval $q_0 = 0.15 - 0.25$ shifts $\sin i$ by $\Delta(\sin i) \lesssim 0.05$, propagating to $\Delta(\log M_{\text{dyn}}) \lesssim 0.05$. For more extreme values $q_0 = 0.50$, this correction can reach $\Delta(\log M_{\text{dyn}}) \approx 0.1$.

Finally, using our dynamical mass measurements, we can compute the DM fractions:

$$f_{\text{DM}} = \frac{M_{\text{DM}}}{M_{\text{dyn}}} = \frac{M_{\text{dyn}} - M_{\text{bar}}}{M_{\text{dyn}}}. \quad (9)$$

All our inferred fractions are calculated within the effective radius r_e since that is where our kinematic measurements are best constrained. We find that 20% of our sample has negative and, therefore, unphysical DM fractions. This fraction drops to 18% (8%) when a deviation from $f_{\text{DM}} = 0$ is required at the level of σ (3σ). These numbers are comparable to those reported in other studies (e.g., Wuyts et al. 2016), and suggest inconsistencies in the modelling of the SEDs and the kinematics, including for instance positive age gradients (D'Eugenio et al. 2021; van Houdt et al. 2021) or non-equilibrium configurations. Although we discuss these systems in the text, unless otherwise mentioned we only consider systems with $f_{\text{DM}} > 0$ for our analyses.

3 DYNAMICAL MASSES & TULLY-FISHER RELATION

In this section, we present the dynamical masses of our systems based on our kinematic modelling (Sec. 3.1), and discuss them within the context of the Tully-Fisher relation at high redshift (Sec. 3.2).

3.1 Dynamical masses

We present our results for the dynamical masses of our galaxies in Fig. 1. We find high dynamical masses spanning $\log(M_{\text{dyn}} [M_{\odot}]) = 9 - 11$, with the overall expected trend of increasing M_{dyn} with M_{\star} , reflecting the baryons tracing the underlying gravitational potential. We find a significant scatter in the dynamical masses at fixed stellar mass, indicative of varying gas and DM contents. To investigate the source of this scatter, we colour-code our galaxies by their offset from the MS (ΔMS), where we adopt the MS from Simmonds et al.

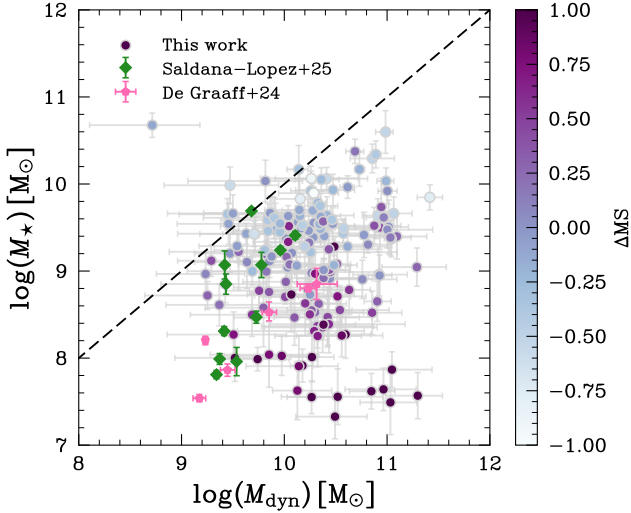


Figure 1. Comparison of the dynamical masses (M_{dyn}) inferred from our modelling of grism data and the stellar masses (M_{\star}) inferred from SED fitting. We colour-code our galaxies based on their offset from the main sequence (ΔMS) as defined by Simmonds et al. (2025). The majority of our systems lie below the one-to-one relation (dashed line), consistent with a significant contribution to the dynamical mass from gas and/or DM. Six galaxies lie on the relation, highlighting discrepancies in the different mass estimates. We compare our values to ionised gas measurements from de Graaff et al. (2024a) and Saldana-Lopez et al. (2025) at similar redshifts.

(2025). We find that galaxies above the MS, which are also typically at lower masses, seem most distant from the 1-1 line, implying a lower stellar contribution to the baryonic and total mass.

We expect the dynamical masses to lie above the stellar masses, as they should also incorporate the gas and DM. We find consistent measurements $M_{\star} < M_{\text{dyn}}$ for the majority of the galaxies in our sample. We discuss the few systems showing unphysical $M_{\text{dyn}} - M_{\star}$ values in more detail in Danhaive et al. (2025a), the discrepancy pointing to problems in the modelling of either or both masses. We compare our sample with measurements from Saldana-Lopez et al. (2025) and de Graaff et al. (2024b) at similar redshifts, and find that they probe the same regions of the parameter space. When combined, these two samples highlight a similar scatter of M_{\star} at fixed M_{dyn} as found in our sample. Overall, these dynamical masses are the key observable that allows us to derive DM fractions (Sec. 2). We note that in a recent study, Phillips et al. (2025) compare intrinsic kinematic measurements from simulations to mock NIRSpect/IFU fits, and find that despite biases in the recovered values of v_{rot} and σ_0 , the dynamical masses remain relatively robust.

3.2 The Tully-Fisher relation (TFR)

Local star-forming disk galaxies exhibit a tight relationship between their stellar mass and circular velocity (v_{circ} , Eq. 7), namely the TFR relation. This relation is typically parametrised as a power law, $M \propto V^a$, or

$$\log M_{\star} = a \cdot \log v_{\text{circ}} + b, \quad (10)$$

where a is the slope and b is the zero-point offset, and M_{\star} is in units of M_{\odot} and v_{circ} in km/s. This relation is analogous to the $M_{\star} - M_{\text{dyn}}$ relation from Fig. 1, given the fundamental link between circular velocities and dynamical masses (Eq. 8) when assuming

virial equilibrium. By understanding where our galaxies lie on the TFR plane, we can place constraints on their mass content compared to galaxies at lower redshift.

In order to explore the offset between our sample at $z = 4 - 6$ and the sTFR at cosmic noon and in the local Universe, we fit Eq. 10 to our sample with the fixed slope from Reyes et al. (2011) at $z \sim 0$ ($a = 3.60$). For our fit, we use the Bayesian inference package EMCEE (Foreman-Mackey et al. 2013). EMCEE samples the parameter space using an implementation of the affine invariant ensemble sampler for Markov chain Monte Carlo (Goodman & Weare 2010), resulting in posterior distributions for the model parameters. Importantly, it allows us to self-consistently fit for the intrinsic scatter σ_{int} around the relation, assuming that our adopted uncertainties for the various measurements are reliable. We discuss this assumption in Sec. 5.2. For the EMCEE fitting, we assume uniform priors for all of the parameters and conduct the MCMC sampling with 50 walkers, a 2000 step burn-in phase, and 10,000 samples. We thin our chains to remove autocorrelation between samples, checking for convergence in the trace plots and in the effective number of independent samples.

We find the following best fit parameters for the $\log(M_{\star} [M_{\odot}]) > 8$ sample, where we are more complete:

$$a = 3.60 \text{ (fixed)} \quad (11)$$

$$b = 0.76 \pm 0.07 \quad (12)$$

$$\sigma_{\text{int}} = 0.49 \pm 0.06. \quad (13)$$

We plot the results for this fiducial fit at $z \sim 5$ in purple in Fig. 2, and also include a fit for the whole sample in red. The large intrinsic scatter, shown by the shaded regions, reflects that the $z \sim 5$ galaxies in our sample are not settled around the TFR. They are likely undergoing kinematic and/or morphological changes on relatively short timescales, which influence the measured circular velocities at fixed stellar masses. More generally, this implies that galaxies have not yet settled into more stable rotating disks, where the TFR is expected to hold (e.g., Übler et al. 2017).

Despite the lack of a tight TFR in our sample, we explore the evolution of the zero-point offset b from $z \sim 0$ (Reyes et al. 2011) and $z \sim 1 - 3$ (Übler et al. 2017, see also Tiley et al. (2016)) to $z \approx 4 - 6$. Both works adopt the same slope. We find a significant increase in the zero-point offset, $\Delta b \approx -1.3$ dex, between our TFR and the one measured at cosmic noon (Übler et al. 2017). This evolution is more significant than the $\Delta b \approx -0.4$ dex evolution from $z \sim 0$ to cosmic noon. The observed decrease of b with redshift could have (a mixture of) different origins. To visually compare with galaxies at cosmic noon, we plot on Fig. 2 the RC100 sample from Nestor Shchar et al. (2023) at $z = 0.6 - 2.5$. It is clear that these cosmic noon galaxies occupy a different parameter space in the TFR plane, having higher stellar masses ($\log(M_{\star} [M_{\odot}]) \approx 10 - 11$) and lower gas fractions ($f_{\text{gas}} \lesssim 0.5$) than our sample.

First, an increase of gas fractions naturally explains the shift of the TFR to higher circular velocities (at fixed mass). This is because v_{circ} reflects the total mass of the galaxy, both baryons and DM, so if the fraction of stars with respect to the other components decreases, the TFR will shift. In the same way, an increase in the DM fractions can also contribute to this shift. It is also possible that b has a mass dependence, since our sample probes smaller masses than the KMOS^{3D} and RC100 samples. It is expected that gas fractions increase at low stellar masses, naturally biasing the stellar TFR. A larger sample spanning larger redshift and mass ranges would be needed to assess the mass dependence of b .

In light of this, we also explore the bTFR in our sample, but similarly to the sTFR we do not find a tight relation akin to what has been

measured at cosmic noon and the local Universe (McGaugh 2012; Lelli et al. 2016). We also find a similar offset towards higher circular velocities at fixed baryonic mass. Together, these points suggests that DM contributes significantly to the total mass of the galaxies in our sample. This is in contrast to the baryon-dominated galaxies seen at cosmic noon. To correctly measure the bTFR, gas masses would need to be directly measured, which is beyond the scope of this work and our available data.

In terms of intrinsic scatter ($\sigma_{\text{int}} = 0.49 \pm 0.06$), we find that it is roughly twice that reported at cosmic noon ($\sigma_{\text{int}} = 0.22$, Übler et al. 2017), where they also find an increase with respect to the local Universe ($\sigma_{\text{int}} = 0.10 - 0.13$ Reyes et al. 2011). As discussed in Übler et al. (2017), one reason for this could be the fact that galaxies at high-redshift are less settled (Simons et al. 2016), and are seen more often in non-equilibrium states (Covington et al. 2010). Also, we rely on 2D grism data in this work and, hence, suffer from more uncertainties than studies with 3D kinematic data. Furthermore, galaxies at high redshift are smaller and lower mass on average, which makes their kinematics more difficult to constrain.

Finally, we note that the lowest-mass galaxies in our sample, with $\log(M_{\star} [M_{\odot}]) < 8$, distinctively fall off our best-fit relation, with high circular velocities of $v_{\text{circ}} > 150$ km/s despite their low masses. We also fit our full sample, including these $\log(M_{\star} [M_{\odot}]) < 8$ objects, and find a smaller zero-point ($b = 0.59 \pm 0.08$) and a larger intrinsic scatter ($\sigma_{\text{int}} = 0.73 \pm 0.07$). These galaxies also have gas fractions close to 1, and are most likely undergoing starbursts ($\Delta\text{MS} > 0$). It is possible that the circular velocities measured for these systems have a non-negligible contribution from non-circular motions, such as radial inflows and/or outflows of gas. This would also contribute to the large observed scatter. Due to their low stellar masses and, hence, small spatial extent, such effects would be difficult to detect in our modelling. Our sample is in general not complete, so our discussion regarding the TFR aims at comparing our sample’s physical properties with those of galaxies at lower redshift and not fully defining the TFR at $z = 4 - 6$.

4 THE GAS AND DM CONTENT AT $Z > 5$

In this section, we quantify the baryonic and DM content of galaxies at $z = 4 - 6$, using gas and DM fractions derived from our kinematic modelling (Sec. 2). We first study the dependence of these fractions on stellar mass (Sec. 4.1), then we focus on the relation between DM fractions and baryonic surface density in Sec. 4.2. Finally, we put our findings in the context of works at lower redshift to discuss the redshift evolution of DM fractions (Sec. 4.3).

4.1 Baryon content at $z \sim 5$

Fig. 3 shows the inferred gas (f_{gas}) and DM (f_{DM}) fractions as a function of stellar mass for the galaxies in our samples. We note that f_{gas} is defined relative to the baryonic mass (stars + gas), whereas f_{DM} is defined relative to the total mass (DM + baryons). We fit both relations with a power law of the form

$$f(z, M_{\star}) = 1 - 10^{\alpha(\log M_{\star} - 9) + \beta + \gamma(\frac{1+z}{6})}, \quad (14)$$

where α and γ parametrize the mass and redshift dependence, respectively, and β is the normalisation at $\log(M_{\star} [M_{\odot}]) = 9$ and $z = 5$. The power-law shape is consistent with the equation from Tacconi et al. (2020) for the gas fractions. Similarly to the TFR, these fits are done with EMCEE using the same general setup (see Sec. 3). We

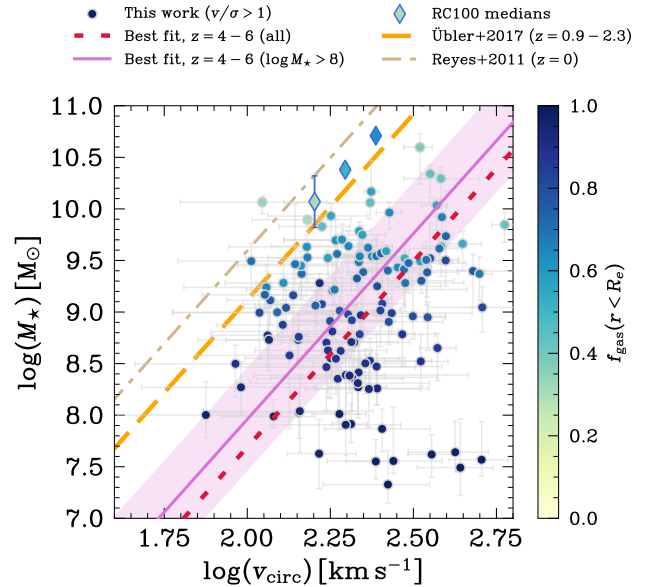


Figure 2. The stellar Tully-Fisher plane for our sample, where the best-fit linear relation for galaxies with $\log(M_{\star} [M_{\odot}]) > 8$ is shown in solid purple (dotted red for the full sample). The circular velocity (v_{circ}) is evaluated at r_e with an asymmetric-drift correction. We find that most of our galaxies lie along the relation, albeit with a large scatter, but the lowest-mass galaxies drop off. We compare our measurements at $z \sim 5$ to the relation found for the KMOS^{3D} $z = 0.9 - 2.3$ star-forming galaxies from Übler et al. (2017) (dashed orange line), and the medians from the RC100 sample (diamonds, Nestor Shachar et al. 2023). We also include the TFR at $z \sim 0$ from Reyes et al. (2011) for reference (dot-dashed tan curve). We fit our data with the same fixed slope as these works, $a = 3.60$, but computing our own zero-point b . We find $\Delta b \approx -1.3$ dex between from $z = 0.9 - 2.3$ to $z = 4 - 6$. The large intrinsic scatter around the relation ($\sigma_{\text{int}} = 0.49 \pm 0.06$; shaded region) indicates that it only beginning to emerge at $z \sim 5$.

summarize the best-fit parameters for both the gas and the DM fractions in Tab. 1. For the gas fractions, we are not able to constrain the intrinsic scatter (σ_{int}) around the best-fit relation. As explained in Sec. 2, we compute the uncertainties on f_{gas} by propagating the uncertainties on both our input parameters and the constant parameters of the Tacconi et al. (2020) scaling relation. This yields relatively large uncertainties of the order of $\Delta f_{\text{gas}} \approx 0.1$ (see characteristic error in Fig. 3). On the other hand, the outputs f_{gas} from the scaling relation vary only a small amount at fixed mass. This is in part due to the small range probed in terms of ΔMS in our sample, since we are not sensitive to galaxies well below the MS. Because of this, our uncertainties are significantly larger than the scatter shown by our inferred f_{gas} , meaning that we cannot constrain σ_{int} .

4.1.1 Gas fractions

As described in Sec. 2, we cannot measure gas masses directly, so we infer them based on the galaxies’ SFRs, stellar masses, and redshifts through the Tacconi et al. (2020) scaling relation. As seen in the top panel of Fig. 3, our galaxies have high predicted gas fractions $f_{\text{gas}} = M_{\text{gas}}/M_{\text{bar}}$, with almost all galaxies having $f_{\text{gas}} > 0.5$. These systems have more gas than stars in their central region $r < r_e$. These high gas fractions are driven in part by the high SFRs, since gas must accrete onto the galaxy to cool and fuel star formation. Gas fractions are also expected to be overall higher at high redshift, but we cannot constrain the redshift dependence of f_{gas} due to the small

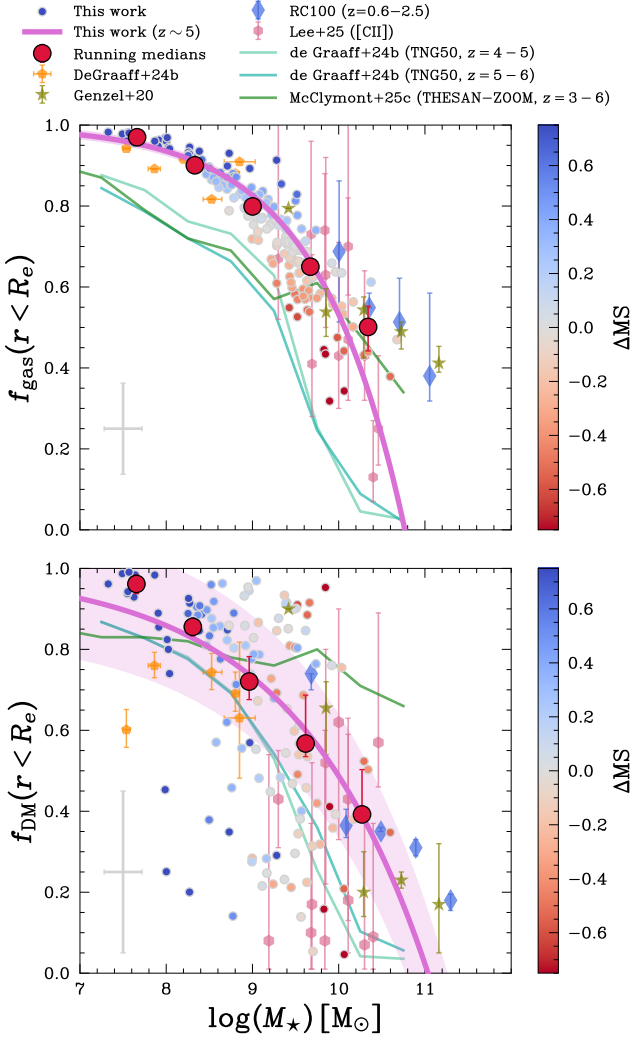


Figure 3. Gas (top) and DM (bottom) fractions (within r_e) as a function of stellar mass, with the characteristic uncertainty shown in grey. The $f_{\text{gas}}(r < r_e)$ (Eq. 4) is computed using the sSFR, redshift, and stellar mass of each galaxy following Tacconi et al. (2020). The $f_{\text{DM}}(r < r_e)$ is computed using M_{gas} along with M_{dyn} and M_{\star} as shown in Eq. 9. We fit our data with a power-law (solid purple line) for both relations, showing the intrinsic scatter (shaded region) only for f_{DM} . We cannot constrain σ_{int} for f_{gas} due to the inferred uncertainties being significantly larger than the scatter in the outputs of the Tacconi et al. (2020) scaling relation for our sample (see Sec. 4.1.1). We compare our results with measurements from Genzel et al. (2020) (green stars) and Nestor Shachar et al. (2023) (RC100; blue diamonds) at cosmic noon and de Graaff et al. (2024a,b) (orange pentagons) and Lee et al. (2025) (pink hexagons) at high redshift. For most of our sample, we find high gas and DM fractions $f > 0.5$. We find relatively good agreement with median trends from the THESAN-ZOOM simulations (green solid line; McClymont et al. 2025c) and the TNG50 simulations (blue solid lines; de Graaff et al. 2024b).

redshift range probed in this work. However, as expected, our inferred dependence of $\gamma = -0.36 \pm 0.45$ is consistent with its counter-part in the Tacconi et al. (2020) scaling relation ($D = -0.41 \pm 0.03$), albeit with very large uncertainties.

We compare our gas fractions with estimates at cosmic noon from Genzel et al. (2020) and Nestor Shachar et al. (2023), which show a large scatter at $\log(M_{\star} [M_{\odot}]) \approx 10 - 11$. Because there is little overlap between this mass range and the one probed in this work, a direct comparison to quantify the independent effects of redshift is

Parameter	f_{gas}	f_{DM}
α	0.43 ± 0.03	0.28 ± 0.05
β	-0.73 ± 0.03	-0.57 ± 0.04
γ	-0.36 ± 0.45	0.34 ± 0.65
σ_{int}	–	0.15 ± 0.02

Table 1. Summary of the parameters for the power-law fit (Eq. 14) to the $f_{\text{gas}}-M_{\star}$ and $f_{\text{DM}}-M_{\star}$ relations (Fig. 3). We cannot constrain σ_{int} for the $f_{\text{gas}}-M_{\star}$ relation due to the inferred uncertainties on f_{gas} being significantly larger than the scatter in the outputs of the Tacconi et al. (2020) scaling relation for our sample (see Sec. 4.1.1 for more details).

not possible. However, their results are consistent with a decrease, on average, of gas fractions with stellar mass.

The high gas fractions at high-redshift are consistent with other predictions of the increase of gas fractions with redshift (Cresci et al. 2009; Genzel et al. 2015; Pillepich et al. 2019). However, this effect appears to also have a strong mass component. The gas fractions found in de Graaff et al. (2024a,b) at $z \approx 6 - 8$ are consistent with our results. In fact, although de Graaff et al. (2024a) use the local relation from Kennicutt (1998) to infer gas masses from SFRs, their measurements lie nicely along our best-fit relation. This suggests that this local relation holds well at $z \sim 6$, at least at the low masses ($\log(M_{\star} [M_{\odot}]) < 9$) probed by their work. The lower gas fractions, derived from [CII] detections, presented in Lee et al. (2025) at $z \sim 4 - 6$ are consistent with our best-fit power-law.

The steep mass dependence of f_{gas} on M_{\star} is also seen in the TNG50 simulations (Pillepich et al. 2019; de Graaff et al. 2024b) and the THESAN-ZOOM simulations (Kannan et al. 2025; McClymont et al. 2025c). At low masses, we find higher gas fractions on average than both of these simulations. This is partly because the relations from Tacconi et al. (2020) and Speagle et al. (2014) do not reach the low mass ($\log(M_{\star} [M_{\odot}]) < 9$) end, and hence the extrapolation could cause an over-estimate of gas fractions at low masses. Importantly, our sample is biased to very star-forming galaxies at the low-mass end, which naturally explains our higher medians.

4.1.2 DM fractions

We now discuss the bottom panel of Fig. 3, where we plot our DM fractions (Eq. 9) as a function of stellar mass. These fractions are computed within the half-light, or effective, radius r_e of the $H\alpha$ emission to avoid extrapolations of our kinematic measurements to larger radii. This implies that the fractions discussed in this work are relevant for the central $r = 1.20 \pm 0.05$ kpc of each galaxy (sample median, Danhaive et al. 2025b). We see a large scatter in the DM content of galaxies at fixed stellar mass, but nonetheless find that low-mass galaxies ($\log(M_{\star} [M_{\odot}]) < 9$) are predominantly DM dominated with $f_{\text{DM}}(r < r_e) > 0.5$. Above $\log(M_{\star} [M_{\odot}]) = 9$, we observe a larger scatter and an overall decline in DM fractions with stellar mass, as is highlighted by the running medians and our best-fit power-law in Fig. 3. We colour-code our galaxies by their offset from the main sequence, but we do not find a clear trend.

We put our f_{DM} measurements in the context of works at cosmic noon, which probe a higher mass range $\log(M_{\star} [M_{\odot}]) \approx 10 - 11$. As shown in Fig. 4.1, Genzel et al. (2020) find that star-forming galaxies at cosmic noon have baryon-dominated cores, with $f_{\text{DM}} \lesssim 0.5$. This is consistent with the extrapolation of our power-law fit to these high masses, suggesting that the mass dependence of f_{DM} exists independently of redshift. In fact, de Graaff et al. (2024b) show with

the TNG simulations that the baryon fraction within 1 kpc, $f_{\text{bar}}(r < 1 \text{ kpc})$, remains constant with redshift at fixed mass. However, it is important to note that our measurements are not at fixed apertures, and we need to take into account the redshift evolution of galaxy sizes (Shibuya et al. 2015; Ward et al. 2024; Danhaive et al. 2025b; Allen et al. 2025; Yang et al. 2025). Nonetheless, our findings suggest that the high DM fractions seen at high- z , both in this work and de Graaff et al. (2024b), are at least in part driven by the lower stellar masses probed compared to lower redshifts. In fact, Lee et al. (2025) probe higher stellar masses on average ($\log(M_{\star} [M_{\odot}]) > 9$) and find DM fractions ranging from $f_{\text{DM}} \approx 0.1$ to $f_{\text{DM}} \approx 0.6$, consistent with the scatter seen in our larger sample at those masses.

We also compare our DM fractions with predictions from the THESAN-ZOOM simulations at $z = 3 - 6$. In general, the simulations are consistent with the majority (60%) of our sample having high DM fractions $f_{\text{DM}} > 0.5$. However, McClymont et al. (2025c) find a weaker mass trend, which does not reproduce the population of $\log(M_{\star} [M_{\odot}]) > 9$ galaxies with lower f_{DM} . This could point to mechanisms which drive DM out from the central regions, such as intense feedback from star formation or black holes (see Sec. 5 for more discussion). Within the simulations, this could also be due to a decrease in the number of galaxies at the high-mass end. Our observed dependence of f_{DM} on M_{\star} is instead more consistent with the trend observed in the TNG50 simulations (de Graaff et al. 2024b).

Some objects have high DM fractions close to $f_{\text{DM}} = 1$. Although these could be caused by an over-estimate of the dynamical mass, they can also point to steepening of the DM halo density profile in the central regions of these galaxies. We explore this in Sec. 5.1. We also find that the inferred f_{DM} fractions for 20% of our sample are unphysical, i.e., $f_{\text{DM}} < 0$. Negative fractions imply that the baryonic mass is larger than the dynamical mass, which could be caused by one or more of the following. The stellar mass inferred from SED fitting could be over-estimated (e.g. due to outshining effects, Sec. 5.2), the dynamical mass from the kinematics fitting could be under-estimated, or the gas fractions inferred from the Tacconi et al. (2020) empirical relation could be over-estimated. Many galaxies in our sample, despite having good fits with low residuals, have clumpy morphologies, which could indicate clumpy SF and/or final stages of a merger. Irregular morphologies can bias the measurement of the rotational velocity due to the simplistic nature of the rotation curve model. Also, if a merger is in fact taking place, the stellar mass may be over-estimated due to the multiple-system nature of the object. In some of the systems, the PROSPECTOR posteriors for the stellar mass are distinctively double peaked, with a lower mass solution that would boost the f_{DM} . Finally, based on the PROSPECTOR-inferred SFHs, many of the systems are either in a burst or just went through a burst, with a peak in SF over a $\sim 5 - 10$ Myr timescale. Especially at low masses, these starbursts can disrupt the ordered rotation of the gas, leading to low and/or bias measurements of v_{rot} .

4.2 Baryonic surface density

In order to investigate the origin of the DM fractions measured in our $z = 4 - 6$ sample, we study their correlation with the baryonic surface density Σ_{bar} , computed within the effective radius of the $H\alpha$ emission, r_e :

$$\Sigma_{\text{bar}}(r_e) = \frac{M_{\text{bar}}(r < r_e)}{2\pi r_e^2}. \quad (15)$$

Our results are shown in Fig. 4, colour-coded by the stellar mass and the gas fraction. The baryonic surface densities of our galaxies

Fit	This work	This work + RC100
α	0.48 ± 0.08	0.28 ± 0.02
β	-0.28 ± 0.04	-0.33 ± 0.02
γ	-0.05 ± 0.58	-0.38 ± 0.07
σ_{int}	0.12 ± 0.03	0.11 ± 0.01

Table 2. Summary of the parameters for the power-law fit to the $f_{\text{DM}} - \Sigma_{\text{bar}}$ relation (where the parameters are defined as in Eq. 14), as shown on Fig. 4.

span a narrow range of $\log(\Sigma_{\text{bar}})[M_{\odot} \text{ kpc}^{-2}] \approx 8 - 9$. We find a strong anti-correlation between f_{DM} and $\log \Sigma_{\text{bar}}$, with Spearman rank correlation coefficient of $\rho = -0.557$ and p-value of $p < 0.001$.

We fit our $f_{\text{DM}} - \log \Sigma_{\text{bar}}$ relation with a power law, replicating the one used for the $f_{\text{DM}} - \log(M_{\star} [M_{\odot}])$ (Eq. 14). This parametrization is motivated by studies of this relation at lower redshift (Wuyts et al. 2016; Genzel et al. 2017; Nestor Shachar et al. 2023), to provide a more straightforward comparison. We present our best-fit parameters in Tab. 2 and plot our best-fit relation in Fig. 4. It is clear that our sample does not follow a clear power-law shape, which is also highlighted by the large intrinsic scatter $\sigma_{\text{int}} = 0.12 \pm 0.03$. The fit is also driven by the higher f_{DM} , which have smaller uncertainties. This causes most of our lower f_{DM} values to have smaller Σ_{bar} than predicted by the best-fit curve.

The tight relation between DM fraction and Σ_{bar} has been found to hold out to cosmic noon in observations (Wuyts et al. 2016; Genzel et al. 2020; Nestor Shachar et al. 2023) as well as in simulations (Übler et al. 2021). This trend links the baryons with underlying the DM, and could be explained by a few different phenomena. The high baryon densities could drive out the DM in the central region through heating. Also, the high densities could be induced by a change in size of the galaxy. In general, for a fixed DM halo and at fixed stellar mass, a higher density of baryons in the centre will naturally result in a lower DM fraction when compared to the same galaxy but more diffuse.

Our measured correlation ($\rho \approx 0.56$) is weaker than the one reported by Nestor Shachar et al. (2023) at $z \sim 2$ ($\rho = 0.64$) and $z \sim 1$ ($\rho = 0.84$). The weakening of the correlation with redshift, as was already observed at cosmic noon, points to an increase of galaxy-to-galaxy diversity. In Fig. 4, we plot the best-fit relation from Wuyts et al. (2016), and we find that our galaxies with the highest DM fractions lie above this relation, as also highlighted by our best-fit relation. At lower DM fractions, our sample aligns better with the relation.

We also perform a fit combining our $z = 4 - 6$ data with the $z = 1 - 2.5$ RC100 data from Nestor Shachar et al. (2023) to obtain better constraints for the redshift evolution of the $f_{\text{DM}} - \Sigma_{\text{bar}}$ relation. Our best-fit parameters are shown on Tab. 2. In our initial fit, the redshift dependence was poorly constrained ($\gamma = -0.05 \pm 0.58$), but when we include the RC100 data, we can constrain the increase of f_{DM} with redshift ($\gamma = -0.38 \pm 0.07$). We investigate the origin of this increase of f_{DM} at fixed Σ_{bar} through the colour-coding by M_{\star} and f_{gas} in the two panels of Fig. 4, and comparing our sample to the Nestor Shachar et al. (2023) sample at cosmic noon. We do not colour-code by r_e because there is little overlap in sizes between the two samples, with our galaxies spanning $r_e \approx 0.3 - 3$ kpc and the RC100 sample $r_e \approx 3 - 10$. The RC100 sample has masses $\log(M_{\star} [M_{\odot}]) \approx 10 - 11$, gas fractions typically $f_{\text{gas}} \lesssim 0.8$, and $r_e > 3$ kpc. It is clear that our sample occupies a different parameter space, with lower masses, higher gas fractions, and smaller sizes. Interestingly, our baryonic surface densities $\log \Sigma_{\text{bar}} \approx 8 - 9$ have significant overlap with those

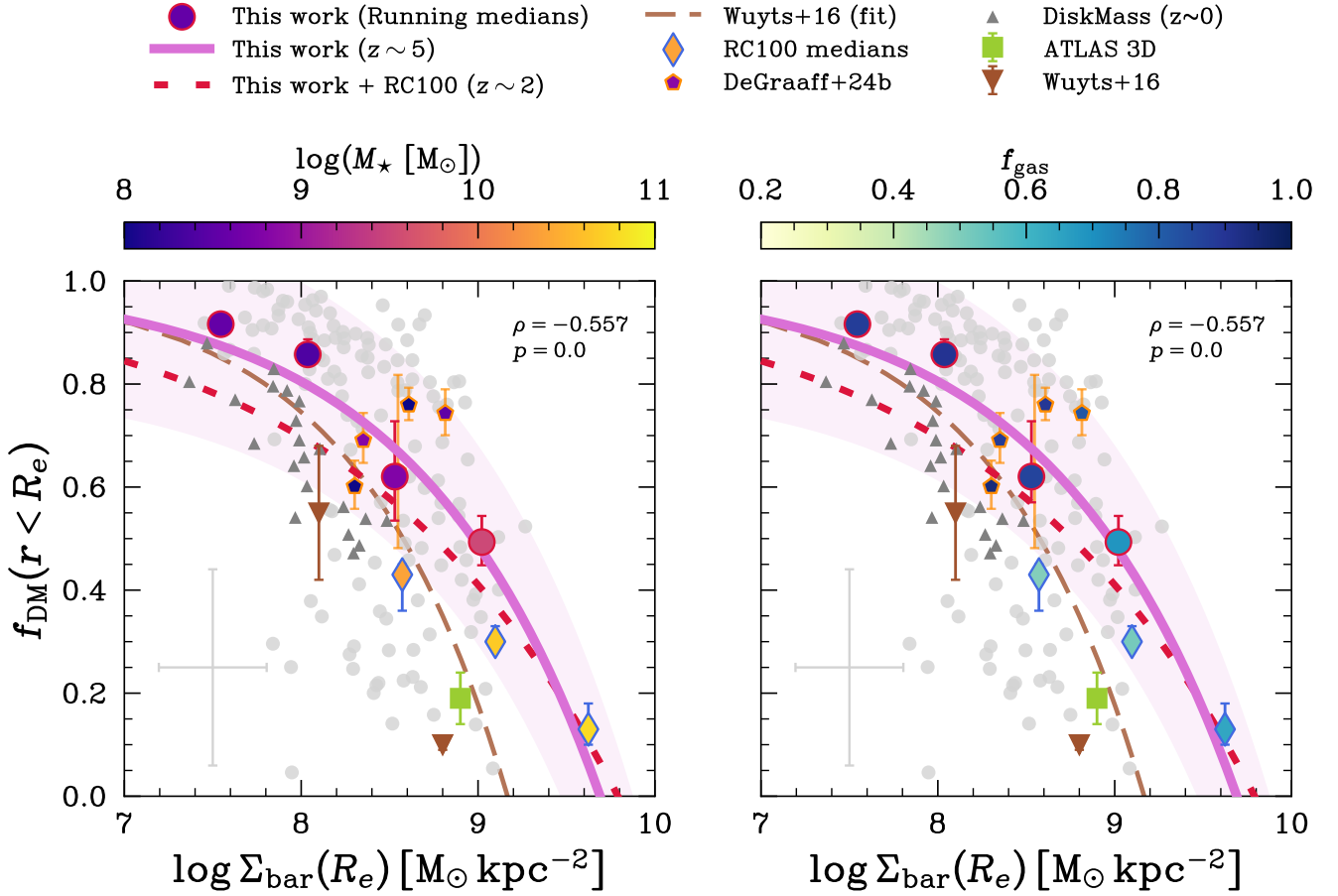


Figure 4. DM fraction as a function of baryonic surface density (Σ_{bar}) for our sample (circles) and samples at lower (diamonds, Nestor Shachar et al. 2023) and similar to higher (pentagons, de Graaff et al. 2024b) redshift. We colour-code points by stellar mass (left panel) and gas fractions (right panel). We show the characteristic uncertainty for our sample in grey. We find a strong negative correlation between f_{DM} and Σ_{bar} ($\rho = -0.551$, $p < 0.001$), with a best-fit relation (solid purple line) steeper than Wuyts et al. (2016) at cosmic noon (dashed brown line), and with an offset. We also plot the best-fit relation obtain when fitting our points with those from Nestor Shachar et al. (2023) (dashed-dotted red line). For comparison, we plot medians from ETGs at $z \sim 0$ from the ATLAS3D survey (purple square; Cappellari et al. 2013a) and LTGs from the DiskMass Survey (grey triangles; Martinsson et al. 2013). Our galaxies agree with Nestor Shachar et al. (2023) at low fractions $f_{\text{DM}} < 0.5$, but lie above the relation at high fractions. The galaxies in our sample are smaller, less massive, and more gas rich than those probed at cosmic noon, driving the apparent shift in the relation.

of cosmic noon galaxies. This implies high densities Σ_{bar} at high redshift, in part driven by the smaller sizes r_e (e.g. Shibuya et al. 2015; Ward et al. 2024). In addition, the gas content is higher and more centrally concentrated, further increasing the baryonic densities in the inner regions. The shift to higher f_{DM} at fixed Σ_{bar} could therefore be driven by the smaller stellar masses, a direct consequence of the stellar-to-halo-mass relation where $M_{\star}/M_{\text{halo}}$ decreases with decreasing M_{\star} (Moster et al. 2010; Behroozi et al. 2010; Tacchella et al. 2018; Behroozi et al. 2019).

The high baryonic surface densities within r_e at high redshift are consistent with the build-up of bulges. In Danhaive et al. (2025b), the study of multi-wavelength sizes and their ratios at $z \sim 5$ supports the growth of galaxies through central starbursts instead of smooth inside-out growth. This is consistent with bulges forming in these relatively low-mass galaxies. At cosmic noon, star-forming galaxies have been shown to predominantly grown inside-out (Nelson et al. 2016), consistent with stars forming in gas disks around an older stellar bulge. The formation of these stellar disks is also reflected in the rapid increase of sizes (r_e) at cosmic noon (Shibuya et al. 2015). In this context, the decrease of f_{DM} , at fixed Σ_{bar} , with cosmic

time reflects the mass build-up of bulges which begin to dominate the central regions of the galaxy. Also, the baryons extend further out into the halo, through inside-out growth, where the DM density decreases, which further decreases f_{DM} .

Assuming galaxies grow along the SFMS, a $\log(M_{\star} [M_{\odot}]) = 9$ galaxy from our sample at $z \sim 5$ would grow to $\log(M_{\star} [M_{\odot}]) \approx 10.5 - 11$ by cosmic noon, similar to the RC100 galaxies. If they maintain high DM fractions in their cores, they would evolve into a separate population from these cosmic noon galaxies, more akin to late-type galaxies (LTGs) in the local Universe (Barnabè et al. 2012; Martinsson et al. 2013). The subset of the galaxies in our sample with $f_{\text{DM}} < 0.5$ would instead be candidate progenitors for the baryon-dominated galaxies at cosmic noon, having also similar gas fractions, as they occupy a similar region on the $f_{\text{DM}} - \Sigma_{\text{bar}}$ plane. As discussed in Nestor Shachar et al. (2023), these galaxies are expected to become ETGs seen in the local Universe (Cappellari et al. 2013a). These different evolutionary tracks are consistent with the large scatter seen in our sample, suggesting a variety of different populations. However, DM fractions are not expected to stay constant within a galaxy’s evolutionary track. In fact, their dependence on mass (Fig.

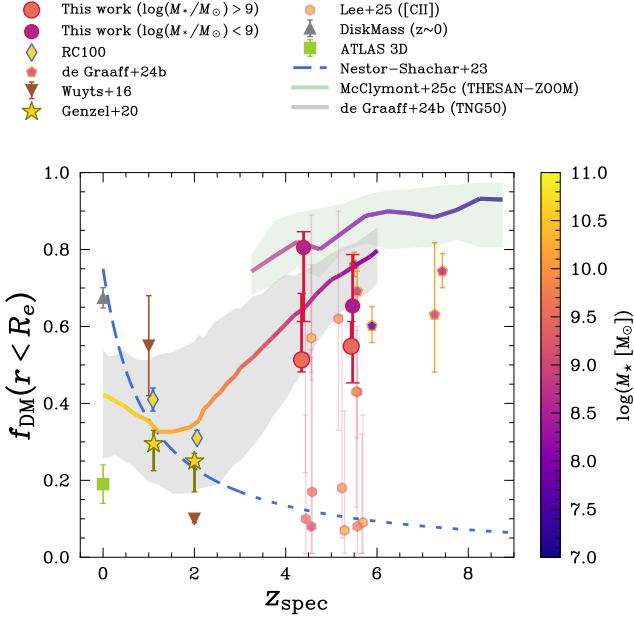


Figure 5. DM fraction as a function of redshift for our sample (circles) and samples from the literature (Nestor Shachar et al. 2023; de Graaff et al. 2024a,b). We plot the evolution measured in Nestor Shachar et al. (2023) (dashed blue line), and its extrapolation to $z > 2.5$ (dotted blue line). Our sample medians lie well above those at cosmic noon, although our sample shows large diversity in f_{DM} and probes $\sim 2 - 3$ dex lower stellar masses. Qualitatively, we compare our medians ($\log(M_{\star} [\text{M}_{\odot}]) \approx 9$) with the median evolution of $f_{\text{DM}}(r < r_e)$ for TNG50 galaxies (de Graaff et al. 2024b) selected at $z = 6$ with $8 < \log(M_{\star} [\text{M}_{\odot}]) < 9$ (thick line with 16th and 84th percentiles shown in the grey shaded region). Similarly, we plot the median evolution for THESAN-ZOOM galaxies (McClymont et al. 2025c) with $\log(M_{\star} [\text{M}_{\odot}]) = 7 \pm 0.5$ at $z = 9$ (thick line with 16th and 84th percentiles shown in the green shaded region). Although we expect redshift evolution of $f_{\text{DM}}(< r_e)$ due to the evolution of sizes with redshift, the strong dependence of stellar mass is evident here.

3) implies that as galaxies grow, their DM fraction changes. Also, the effective radii increase with cosmic time, which also affects the measurements. We investigate the redshift evolution of f_{DM} in the next section.

4.3 Redshift evolution of f_{DM}

In Fig. 5, we plot our inferred DM fractions as a function of redshift. We plot our sample medians at $z = 4.5$ and $z = 5.5$, for the lower-mass ($\log(M_{\star} [\text{M}_{\odot}]) < 9$) and higher-mass ($\log(M_{\star} [\text{M}_{\odot}]) > 9$) galaxies. Although our sample spans a wide range of f_{DM} , we find high fractions on average ($f_{\text{DM}} > 0.5$). For the high-mass galaxies, with median $\log(M_{\star} [\text{M}_{\odot}]) = 9.5$, we find $f_{\text{DM}} = 0.51_{-0.17}^{+0.03}$ and $f_{\text{DM}} = 0.55_{-0.01}^{+0.06}$ at $z = 4.5$ and $z = 5.5$, respectively. For the low-mass galaxies, with median $\log(M_{\star} [\text{M}_{\odot}]) = 8.5$, we find $f_{\text{DM}} = 0.81_{-0.19}^{+0.04}$ and $f_{\text{DM}} = 0.65_{-0.20}^{+0.13}$. In both cases, we do not see evidence for a redshift evolution, as our medians at $z = 4.5$ and $z = 5.5$ are consistent within the uncertainties. This is expected given our poorly constrained γ values (Tab. 1).

We now place our measurements in the context of work at cosmic noon and the local Universe. In the same redshift range $z \approx 4 - 6$, Lee et al. (2025) report a wide range of f_{DM} for their higher mass sample ($\log(M_{\star} [\text{M}_{\odot}]) \approx 9 - 10.5$), but their higher f_{DM} systems are consistent with our high-mass medians. However, they

also report galaxies that have large baryon contents ($f_{\text{DM}} \lesssim 0.2$). We also find similar systems in our sample (Fig. 3) even though our medians lie at higher f_{DM} . The systems from Lee et al. (2025) are therefore consistent with being a subset of the more extensive population probed in this work. At higher redshift ($z \approx 5 - 8$), measurements from de Graaff et al. (2024a,b), who find $f_{\text{DM}} > 0.5$ for their sample of $\log(M_{\star} [\text{M}_{\odot}]) \approx 8 - 9$, are broadly consistent with our low-mass medians. On the other hand, the medians for $\log(M_{\star} [\text{M}_{\odot}]) \approx 10 - 11$ galaxies at cosmic noon (Genzel et al. 2020; Nestor Shachar et al. 2023) show low DM fractions ($f_{\text{DM}} \approx 0.2 - 0.4$). When combining all of these measurements together, the resulting picture suggests that mass plays a significant role in determining the DM content within the central regions of galaxies. The massive systems at cosmic noon are predominantly baryon-dominated, as is also seen in more massive systems at $z \sim 5$. On the other hand, low-mass galaxies seem more DM-dominated.

To further investigate this, we plot the median tracks from the TNG50 (de Graaff et al. 2024b) and THESAN-ZOOM (McClymont et al. 2025c) simulations. Specifically, for TNG50, we plot the median evolution of $f_{\text{DM}}(r < r_e)$ for galaxies selected at $z = 6$ with $8 < \log(M_{\star} [\text{M}_{\odot}]) < 9$. The THESAN-ZOOM track is computed as a median from galaxies with $\log(M_{\star} [\text{M}_{\odot}]) = 7 \pm 0.5$ at $z = 9$. This comparison with simulations is qualitative, as the radii r_e are defined and measured differently in observations and simulations. Observationally, we are only able to measure the 2D half-light radius, whereas simulations define r_e as the 3D stellar half-mass radius. The choice of r_e will have an impact on the measured fractions and the derived comparisons. Despite this not being an apples-to-apples comparison, it is informative to explore its implications.

As discussed in de Graaff et al. (2024b), TNG50 predicts that low-mass galaxies are DM dominated at every epoch, and the observed evolution of f_{DM} is driven by the masses probed. In fact, the tracks on Fig. 5 show that a single galaxy goes from being DM-dominated at $z \sim 6$ to being baryon-dominated at $z \sim 2$. This is also consistent with the tracks from THESAN-ZOOM, although these simulations only reach $z = 3$. This has strong implications for the evolutionary tracks of galaxies, since it suggests that the DM-dominated low-mass galaxies probed at high redshift are direct progenitors of the baryon-dominated cosmic noon galaxies. From cosmic noon, the DM-dominated systems settle as the DM-dominated LTGs in the local Universe, whereas the baryon-dominated systems could deplete their gas and settle in to the ETGs (Nestor Shachar et al. 2023). A detailed forward-modelling of the simulations is needed to conduct a better comparison with the increasing number of observed fractions.

5 DISCUSSION

The study of DM fractions, within the effective radius, at cosmic noon ($z \approx 1 - 3$) unveiled that the massive ($\log(M_{\star} [\text{M}_{\odot}]) = 10 - 11$) star-forming galaxy population is predominantly baryon-dominated (Genzel et al. 2017, 2020; Nestor Shachar et al. 2023). In this work, we push the study of f_{DM} to $z \approx 4 - 6$, where we are directly probing progenitors of these cosmic noon systems. In Sec. 4.1 and Sec. 4.2, we presented our DM fractions and their dependence on stellar mass and baryonic surface density, investigating the physical drivers for the offsets we observe with respect to cosmic noon galaxies. In Sec. 4.3, we put our measured f_{DM} in the context of galaxies across cosmic time and predictions from tracks of cosmological simulations.

In this section, we qualitatively explore what our measurements can teach us about the underlying DM halo, and specifically what constraints we can place on the shape of its density distribution in

the central regions (Sec. 5.1). From this, we hope to shed light on the consistency of different estimations of the galaxy-halo connection. We also discuss the different sources of uncertainties in our baryonic (Sec. 5.2) and DM (Sec. 5.3) mass measurements. Finally, we also consider the contribution of black holes to our measured fractions in Sec. 5.4.

5.1 Empirical model predictions

Our modelling, which is limited to probing rotational curves out to $\approx 1 - 2 r_e$, does not allow for a detailed recovery of the underlying DM density profiles of our galaxies. Ideally, rotation should be probed further out to several r_e . However, the measure of the DM fractions within r_e can provide constraints on the DM density profile via comparisons to empirical predictions, which require various assumptions. We explore these constraints in this section, but caution that they remain qualitative and reliant on assumed relations.

The stellar-to-halo mass (SMHM) relation has been studied in detail both in empirical models (Behroozi et al. 2019; Tacchella et al. 2018) and in simulations (Ceverino et al. 2017; Ma et al. 2018), with constraints from observations (Kravtsov et al. 2018; Girelli et al. 2020; Shuntov et al. 2022, 2025). This relation links the halo mass of galaxies to their stellar mass at a given redshift, allowing us to estimate the halo masses for the galaxies in our sample. In order to estimate the halo masses for our galaxies, we adopt the Behroozi et al. (2019) SMHM relation, which has a double power-law shape with an added Gaussian:

$$\log_{10} \left(\frac{M_*}{M_1} \right) = \varepsilon - \log_{10} \left(10^{-\alpha x} + 10^{-\beta x} \right) + \gamma \exp \left[-0.5 \left(\frac{x}{\delta} \right)^2 \right] \quad (16)$$

where $x \equiv \log_{10} \left(\frac{M_{\text{peak}}}{M_1} \right)$, M_{peak} is the peak halo mass and M_1 is a characteristic mass. The free parameters M_1 , ε , α , β and γ all have redshift-dependent expressions, and δ is a constant. Once we have inferred the halo mass by numerically solving Eq. 16, we can derive the corresponding virial radius:

$$R_{\text{vir}} = \left(\frac{4 \pi 200 \rho_c}{3 M_{\text{halo}}} \right)^{-1/3}, \quad (17)$$

since R_{vir} is defined as the radius where the density is 200 times the critical density ρ_c of the Universe at that redshift, and M_{halo} is the DM mass within the virial radius. For the shape of the DM density profile, we assume a generalized Navarro–Frenk–White (NFW, Navarro et al. 1997) profile:

$$\rho_{\text{DM}}(r) = \frac{\rho_0}{(r/r_s)^\alpha (1 + r/r_s)^{3-\alpha}}, \quad (18)$$

where $\alpha = 1$ corresponds to a classic NFW profile. Given these assumptions, we can constrain the value of α needed to reproduce our measured DM fractions f_{DM} within the effective radius. We restrict our values between $\alpha = 0$ and $\alpha = 3$, above (below) which the profile becomes convex (concave) in logarithmic space. In fact, for $\alpha > 3$, Eq. 18 develops an upturn near $r = r_s$, as the outer slope $(3 - \alpha)$ becomes negative. Conversely, when $\alpha < 0$, the inner slope (α) becomes negative, producing a downturn at $r = r_s$. Within the allowed range $0 \leq \alpha \leq 3$, the profile smoothly transitions from a nearly flat core ($\alpha = 0$) to a progressively steeper slope that becomes (log-)linear at $\alpha = 3$.

The only additional unknown is the concentration c , defined as

$$R_{\text{vir}} = c R_s \quad (19)$$

where R_s is the scale radius. Given our other assumptions, the value of c effectively re-normalizes the predicted DM fractions for all of our systems, increasing them as c increases. DM only simulations predict low concentrations at $z \sim 5$ (Dutton & Macciò 2014), so we set $c = 5$.

In Fig. 6, we present the estimated values of α needed to reproduce our measured DM fractions within the effective radius. We find that $\approx 30\%$ of our sample lies below $\alpha = 1$, implying that their DM fractions are best reproduced by a profile that is more cored than the classical NFW. Evidence for DM cores has already been found at cosmic noon (Genzel et al. 2020; Nestor Shachar et al. 2023), where samples are predominantly baryon-dominated and require cored profiles to reproduce their low f_{DM} . Aside from more extreme solutions such as the modification of the nature of DM (Hu et al. 2000; Calabrese & Spergel 2016) or of our gravity model (Milgrom 1983), a more natural explanation for such cores is a strong interaction between the baryons and the DM within galaxies. Specifically, this would require kinetic heating of the DM in the central regions to drive it outwards. This could be achieved through effective feedback mechanisms from star formation and black holes. Another possibility is that some of these low f_{DM} galaxies are in a post-merger phase, with disturbed kinematics and diffused DM haloes. This is plausible given that most of the galaxies in the $\alpha < 0$ region have higher stellar masses ($\log(M_* [M_\odot]) > 9$).

On the other hand, high central baryonic concentrations are expected to perturb the underlying DM distribution and pull the DM towards the centre, increasing the "cuspieness" of its density profile. This phenomenon is called adiabatic contraction (Blumenthal et al. 1986), and is represented by the $\alpha > 1$ region of Fig. 6. For galaxies in this region, adiabatic contraction is needed to explain the high f_{DM} values measured in this work. Interestingly, this under-prediction of f_{DM} , compared to our observations, holds for many other SMHM relations from the literature which typically lie above the Behroozi et al. (2019) one (e.g. Tacchella et al. 2018). In order to bridge some of the discrepancies between the model predictions and our measurements, a lower SMHM relation at high redshift would be needed. This problem is emphasized by recent predictions from observations and simulations of high DM fractions in low-mass galaxies (de Graaff et al. 2024b; McClymont et al. 2025c). However, it is important to note that our high $\alpha \gtrsim 1.5$ values suffer from large uncertainties that make them consistent with $\alpha \approx 1.5$. These stem from the smaller masses of these systems, which make their morphology and kinematics more difficult to constrain.

We colour-code our points in Fig. 6 by their SFHs, parametrized by the ratio of SFR averaged over 10 and 100 Myr. Galaxies with rising SFHs will have positive values of $\text{SFR}_{10}/\text{SFR}_{100}$, whereas galaxies with falling SFHs will show the opposite behaviour. In order to visually assess the presence of an underlying trend, we combine our points in larger bins and use the LOESS method (Cappellari et al. 2013b) to average over single objects and obtain mean estimates for the full sample. We can see a trend of galaxies going through a burst $\log \text{SFR}_{10}/\text{SFR}_{100} \gtrsim 0.4$ having preferentially higher values of α . This apparent correlation supports the adiabatic contraction scenario that would occur with the inflow of baryons to the central regions during a burst, during which the gas content of the galaxy contracts (Dekel & Burkert 2014; Tacchella et al. 2016b; McClymont et al. 2025b). When feedback from the star formation kicks in, driving the gas out of the centre and temporarily quenching star formation, galaxies begin to move back down towards the MS $\log \text{SFR}_{10}/\text{SFR}_{100} < 0$. These galaxies appear to preferentially have cored profiles, consistent with kinetic heating of the DM. This interpretation would imply the interaction of baryons and DM on relatively short timescales ($t \approx 100$

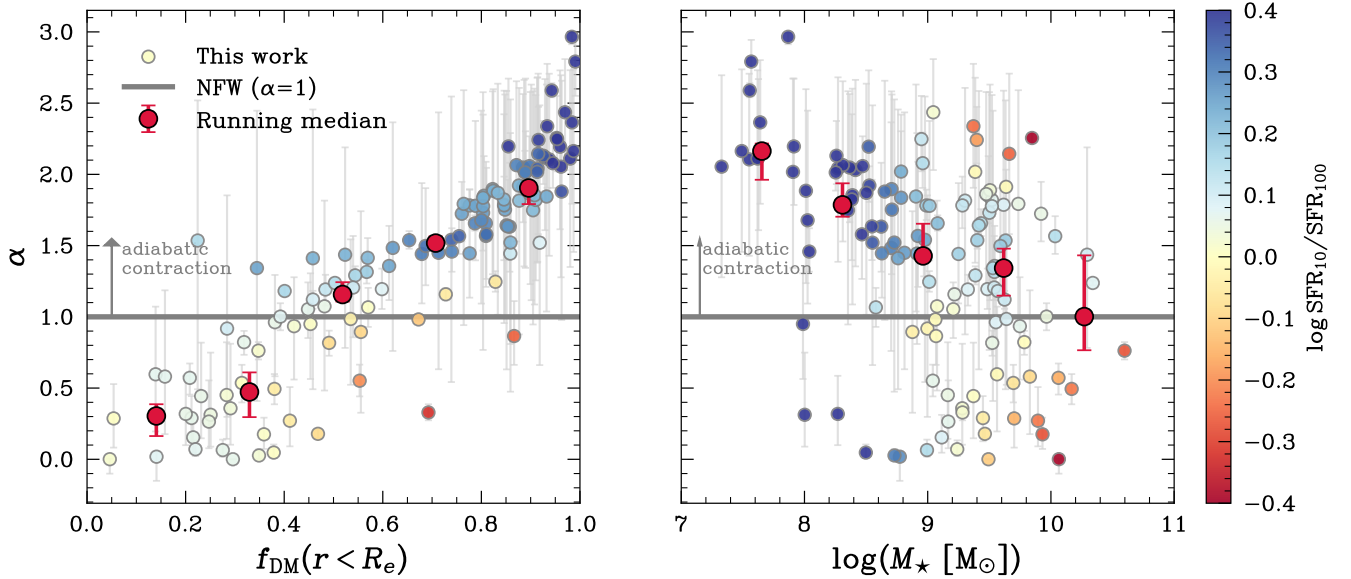


Figure 6. Estimated slope α of the inner DM density profile for a modified NFW distribution (Eq. 18) as a function of measured DM fractions (left) and stellar mass (right). A value of $\alpha = 1$ represents the classical NFW profile, whereas $\alpha < 1$ corresponds to a cored profile, and $\alpha > 1$ to a cuspy profile. Under the assumed SHMR and concentration ($c = 5$), we find that low-mass galaxies with high f_{DM} are associated with cuspy distributions, converging towards an NFW-like profile at higher masses with a scatter at least in part driven by their star-formation state. To highlight this, we colour-code the galaxies by the ratio of their SFR averaged over 10 and 100 Myr, $\text{SFR}_{10}/\text{SFR}_{100}$, applying LOESS smoothing (Cappellari et al. 2013b). Galaxies going through a burst of star formation ($\log \text{SFR}_{10}/\text{SFR}_{100} \gtrsim 0.4$) have preferentially high values of α , which supports the adiabatic contraction scenario.

Myr), which has yet to be thoroughly explored in cosmological simulations. Interestingly, we also find that the values of α correlate with the Sérsic index n measured from the stellar light distribution in the UV (Fig. A1). Galaxies with cuspy DM profiles also have steeper central light profiles, with $n \sim 4$, which could point to interactions between the two components.

We find that low-mass galaxies $\log(M_{\star} [M_{\odot}]) < 9$ have cuspy profiles, while higher mass galaxies seem to converge towards NFW profiles ($\alpha = 1$) with scatter driven by their star-formation state (parametrized by $\text{SFR}_{10}/\text{SFR}_{100}$). This is not necessarily intuitive given the initial discovery of cored systems in dwarf galaxies in the local Universe. However, this can be reconciled when considering burstiness. At high redshift, galaxies have been shown to grow through bursts of star formation (e.g. Faucher-Giguère 2018; Tacchella et al. 2020; McClymont et al. 2025a; Simmonds et al. 2025) at all masses. These bursts are tied to the formation of cores through energetic stellar feedback smoothing the DM profile in the central regions of galaxies. The more massive galaxies in our sample will have undergone more bursts in their lifetime, leading to a flattening of their DM profiles and resulting in the more cored profiles we predict in this work. Also, these galaxies could undergo breathing cycles of compaction phases (Tacchella et al. 2016a; El-Badry et al. 2016). Interestingly, Kohandel et al. (2025) find that one of their most massive galaxies ("Amaryllis", $\log(M_{\star} [M_{\odot}]) = 10.3$ at $z = 7$) has a cored inner DM density profile which reflects the cusp-flattening impact of baryonic feedback.

In the local Universe, star formation is smoother, with massive star-forming galaxies growing more smoothly inside out once their central bulges have developed. These massive galaxies undergo long-lived stable growth episodes that could allow their DM profile to stabilise around NFW profiles. On the other hand, dwarf galaxies still have bursty star formation (Hopkins et al. 2014; Hayward & Hopkins 2017; Hopkins et al. 2023), giving rise to their cores. It is

also important to once again consider the evolution of sizes. These dwarf galaxies have larger radii than low-mass galaxies at the same mass in our sample. This naturally implies higher concentrations, which could fuel processes of adiabatic contraction for which we see evidence in Fig. 6.

Finally, we assess how sensitive our results are to the adopted assumptions and discuss their potential impact on our conclusions. Starting with the concentration, changing the value of c affects the distribution of α we find. Specifically, higher concentrations $c > 5$ require more galaxies to have cored profiles $\alpha < 1$ in order to reconcile the predicted fractions f_{DM} with our measured ones. In contrast, lower concentrations, $c < 3$, would have the opposite effect. The most important choice is the SMHM function, which directly affects the normalization of our profiles and, hence, of the α values that we infer. Studies based on simulations and empirical models at high redshift suggest that the normalization of the SMHM relation is higher than the Behroozi et al. (2019) one assumed in this work (e.g. see Tacchella et al. 2018). This means that the halo mass M_{halo} at fixed stellar mass M_{\star} is lower than predicted by the Behroozi et al. (2019) relation, meaning our profiles would need to be even cuspy (higher α) to reproduce our high f_{DM} values. A last assumption is the choice of profile for the fit, as other profiles such as the Einasto profile (Einasto 1965), have also been shown to provide good fits to DM profiles in cosmological simulations (Dutton & Macciò 2014). We explored this profile and found no significant change in the observed trends of cuspieness with f_{DM} , $\text{SFR}_{10}/\text{SFR}_{100}$, and M_{\star} . However, our points become more scattered in these parameter spaces. We chose to study the modified NFW profile in the most detail because of the direct comparison it offers with the NFW ($\alpha = 1$) case (Eq. 18).

Although it is informative to discuss empirical model predictions in the context of our results, it is also important to discuss caveats of the measurements that could potentially reconcile our inferred profiles with shapes closer to NFW. We discuss these in the next two

sections, focusing on the uncertainties in the baryonic and the DM contents.

5.2 Uncertainties in the baryonic content

When calculating baryonic masses needed to infer gas and DM fractions, we need to make some assumptions, of which we will now discuss the implications. First, the stellar mass is inferred using the SED-fitting code `PROSPEROR`, a method with many advantages, but also some degeneracies. We attempt to break some of the degeneracies by fixing the redshift to the grism spectroscopic redshift, and by simultaneously fitting the photometry with the line fluxes of the available emission lines (see Sec. 2). Despite this, we are not fitting spectra and do not have strong constraints for all emission lines, for instance, those constraining nebular metallicities and dust content. Furthermore, our S/N cut implies selecting galaxies whose young stellar population is dominating the SED. This may hamper the detection of the underlying population of older stars, and hence constraining the full SFH. This effect is called ‘outshining’ and can cause an underestimate of the stellar masses, effectively only attributing the stellar mass to the more visible young stellar population (Bell & de Jong 2001; Maraston et al. 2010; Leja et al. 2019; Tacchella et al. 2023; Giménez-Arteaga et al. 2023). This would directly affect the measurements of $f_{\text{DM}} < 0$, alleviating the tension by increasing the total baryonic mass.

Uncertainties in the stellar mass and SFRs are propagated into the gas mass estimates derived using the scaling relation by Tacconi et al. (2018, 2020). This relation is calibrated out to $z \sim 5.5$, and should hence provide a better estimate of the gas in our galaxies than relations calibrated at much lower redshifts (e.g. Kennicutt 1998). Nonetheless, the use of scaling relations does not necessarily encompass the large variety of gas fractions observed at fixed mass (e.g. McClymont et al. 2025c), and could introduce biases. Importantly, the Tacconi et al. (2020) relation is only calibrated above $\log(M_{\star} [\text{M}_{\odot}]) \gtrsim 9$. The extrapolation to the lower masses in our sample results in very high gas fractions $f_{\text{gas}} \sim 1$.

5.3 Uncertainties in the DM content

The kinematic measurements, described in Danhaive et al. (2025a), are the main factor driving the measurement of f_{DM} through their estimate of the dynamical mass. The key assumption made when deriving the dynamical mass is that the measured velocity gradients are tracing rotation of the gas around the galaxy. However, especially at low masses, we cannot rule out the contribution of non-circular motions, typically in the form of outflows (Carniani et al. 2024; Ivey et al. 2025), to our measurement of velocity gradients and dispersions. Such a contribution would bias both quantities to higher values and unphysically boost the inferred dynamical masses, and hence the DM fractions. Also, albeit of smaller importance, the circular velocities needed to compute the dynamical masses are inferred assuming a virialised rotating disk with an exponential light profile. For galaxies with larger Sérsic indices, this assumption can lead to biased results. Furthermore, for pressure dominated systems, the choice of the pressure support term multiplying the σ_0 in Eq. 7 can lead to over or under-estimates of the circular velocity (see Price et al. 2022, for detailed analysis).

For the derived relations for both the gas and importantly the DM fractions, we note that we suffer from incompleteness at the low-mass end ($\log(M_{\star} [\text{M}_{\odot}]) < 9$), which could significantly bias our results. In order to obtain meaningful (i.e. resolved) kinematic

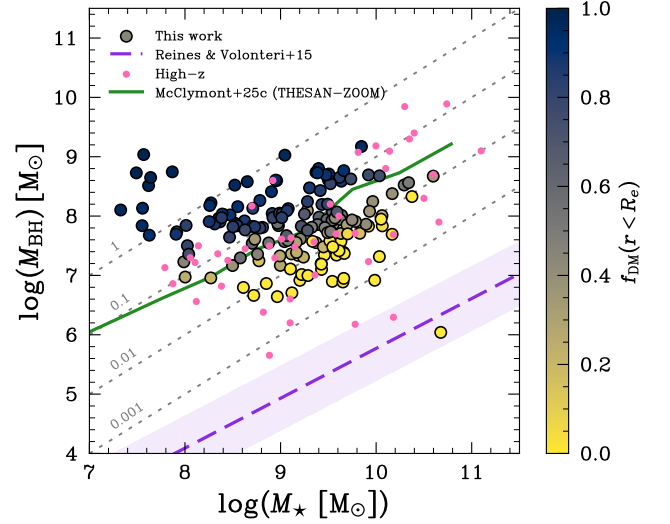


Figure 7. Predicted black hole masses M_{BH} , assuming the local $M_{\text{BH}} - M_{\text{dyn}}$ relation from Kormendy & Ho (2013), as a function of stellar mass (circles). We compare our measurements with the overmassive black holes reported at high redshift ($z \approx 4 - 11$) from *JWST* (pink dots; Carnall et al. 2023; Kokorev et al. 2023; Harikane et al. 2023; Matthee et al. 2024; Übler et al. 2023; Maiolino et al. 2024b,a; Übler et al. 2024; Greene et al. 2024; Furtak et al. 2024; Juodžbalis et al. 2024; Natarajan et al. 2024), which lie well above the local relation (purple dashed line; Reines & Volonteri 2015). The dashed grey lines represent constant ratios of M_{BH}/M_{\star} . We find excellent agreement with the parameter space spanned by these sources, suggesting the shift in the $M_{\text{BH}} - M_{\star}$ relation is consistent with the high gas and DM fractions found in high redshift galaxies. This is consistent with results from McClymont et al. (2025c) following a similar approach to this work but with the THESAN-ZOOM simulations.

measurements for low-mass systems, they need to be not only bright in $\text{H}\alpha$, but also have relatively large rotational velocity and/or velocity dispersions. This could cause our f_{gas} to be biased high (due to the high SFR requirement for the bright $\text{H}\alpha$) as well as our f_{DM} (due to the high circular velocities). Accounting for these selection effects would move our observed medians closer to the simulations in Fig. 3. Within the paper, we discuss the observed trends, but cannot make definitive conclusions about the behaviour at the low masses. This also translates to incompleteness for galaxies with low baryonic surface densities.

In this discussion, there is a last component that we have not considered, namely the presence of BHs in our galaxies. We investigate this possibility in the next section.

5.4 Overmassive BHs

Although BHs typically represent a small fraction of the total mass, with $M_{\text{BH}}/M_{\star} < 1\%$ at $z \sim 0$ (Reines & Volonteri 2015), they could have non-negligible effects on the kinematics of their host galaxies through potentially disruptive feedback mechanisms. Furthermore, many recent studies have reported over-massive BHs in the early Universe, with high M_{BH}/M_{\star} ratios (Carnall et al. 2023; Kokorev et al. 2023; Harikane et al. 2023; Übler et al. 2023; Maiolino et al. 2024b,a; Übler et al. 2024; Furtak et al. 2024; Natarajan et al. 2024; Juodžbalis et al. 2025a) and in some cases even high $M_{\text{BH}}/M_{\text{dyn}}$ ratios (D’Eugenio et al. 2025; Ji et al. 2025; Juodžbalis et al. 2025b) relative to the local scaling relations.

In order to investigate the presence of BHs in our galaxies, and

quantify their potential contributions to our measured DM fractions, we derive BH masses using the $M_{\text{BH}} - M_{\text{dyn}}$ relations from [Kormendy & Ho \(2013\)](#), which has been shown to hold at high redshift for most cases ([Maiolino et al. 2024b](#); [Juodžbalis et al. 2025b](#)). We show our results on Fig. 7.

We find BH masses spanning a wide range ($\log(M_{\text{BH}} [\text{M}_{\odot}]) = 6.5 - 9$) and BH-to-stellar mass ratios ($M_{\text{BH}}/M_{\star} = 0.001 - 1$). Interestingly, our sample overlaps with most of the over-massive BHs reported at high redshift. This suggests that, given a fixed $M_{\text{BH}} - M_{\text{dyn}}$ relation like we have assumed here, these over-massive black holes (relative to the $M_{\text{BH}} - M_{\star}$ plane) are a natural consequence of the high gas and DM fractions found at high redshift (Fig. 4.1). This is consistent with the results from [McClymont et al. \(2025c\)](#), who applied a similar semi-empirical approach to the THESAN-ZOOM simulations, whose model does not include black holes, to predict black hole masses in the post-processing. Our results imply that ratios of $M_{\text{BH}}/M_{\star} \approx 0.1$ would be common at high-redshift, and that black holes grow faster at early times, in comparison to the stellar content, than at late times. Because both growth mechanisms require gas inflow, the gas must collapse enough to accrete on to the black hole but without forming many stars. Black hole growth would need to differ at high redshift in order to reproduce these high M_{BH}/M_{\star} ratios. However, confirming the presence of black holes at high redshift has proven difficult with our current emission line diagnostics (e.g. [Mazzolari et al. 2024](#); [Scholtz et al. 2025](#); [Ivey et al. 2025](#)), and various emission line ratios need to be detected spectroscopically, which we do not probe with the grism data used in this work. Also, many models expect that the bulk of the BH population at high- z should be dormant (e.g. [Schneider et al. 2023](#); [Trinca et al. 2024](#)), with short duty cycles for accretion, meaning that we would not expect to see evidence of accreting BHs.

We note that the lower mass systems $\log(M_{\star} [\text{M}_{\odot}]) < 8$ in our sample have abnormally high dynamical masses, leading to high predictions of M_{BH} , pointing to a likely contribution from non-circular motions, as also shown in Sec. 3. For the remainder of the systems, our findings imply that the BHs could have a significant impact on their host galaxies. Although including their masses in our calculation of f_{DM} does not strongly affect these measurements, due to the small $M_{\text{BH}}/M_{\text{dyn}}$ values ([Kormendy & Ho 2013](#)), those who are accreting could affect the kinematics of the surrounding gas and introduce biases in the measurement of M_{dyn} . If present, these AGNs could be categorized as Type-II, narrow-line AGNs, and hence would not be detected through the broadening of emission lines caused by the broad-line region. Nonetheless, AGN-driven outflows in low-mass galaxies would have similar velocities to those measured in this work ($v \sim 100 - 200$ km/s, e.g. [Ivey et al. 2025](#)), and could hence boost our measured DM fractions.

6 SUMMARY & CONCLUSIONS

This work presents the dynamical mass measurements of 163 $\text{H}\alpha$ emitters at $z \approx 4-6$ from the FRESCO and CONGRESS JWST grism surveys in the GOODS fields. We model the kinematics of the $\text{H}\alpha$ emission line using forward-modelling and fitting of the grism data with GEKO ([Danhaive & Tacchella 2025](#)), recovering in particular rotational velocities and velocity dispersions. Using our measured dynamical masses from our modelling, stellar masses inferred from SED modelling, and gas masses estimated from the [Tacconi et al. \(2020\)](#) scaling relation, we obtain the gas fractions (f_{gas}) and DM fractions (f_{DM}) within the $\text{H}\alpha$ half-light radius (r_e). We summarize our main findings here:

- The $\log(M_{\star} [\text{M}_{\odot}]) \approx 7 - 10$ star-forming galaxies in our sample have relatively high dynamical masses in the range $\log(M_{\text{dyn}} [\text{M}_{\odot}]) \approx 9 - 11$. At fixed stellar mass, there is large scatter in the dynamical masses, indicative of unsettled kinematics. This scatter naturally manifests itself in the Tully–Fisher plane, suggesting that the relation is only beginning to emerge at $z \sim 5$.

- Our galaxies have, on average, high molecular gas and DM fractions, with sample medians $\langle f_{\text{gas}} \rangle = 0.77$ and $\langle f_{\text{DM}} \rangle = 0.73$. We find that $\approx 67\%$ of our galaxies are DM dominated with their $r_e \sim 0.5 - 1$ kpc, $f_{\text{DM}} > 0.5$. Nonetheless, our fractions f_{DM} span the full range of the parameter space.

- We find evidence for a negative dependence of f_{DM} on stellar mass M_{\star} as parametrized by Eq. 14. Specifically, we find $\alpha = 0.28 \pm 0.05$, with low-mass ($\log(M_{\star} [\text{M}_{\odot}]) < 9$) galaxies showing high DM fractions and higher mass galaxies ($\log(M_{\star} [\text{M}_{\odot}]) > 9$) showing a larger diversity, with typically lower f_{DM} .

- We find an anti-correlation ($\rho = -0.56, p < 0.001$) between f_{DM} and the baryonic surface density Σ_{bar} within r_e , consistent with but weaker than its counterpart at cosmic noon and the local Universe. The galaxies in our sample have high baryonic surface densities comparable to those of more massive galaxies at cosmic noon, caused by their compactness and high central gas fractions.

- Our high DM fractions are consistent with the predicted progenitor populations of $z \sim 2$ baryon-dominated systems, as shown by a comparison with the TNG50 and THESAN-ZOOM simulations. These high fractions are expected for low-mass galaxies at all redshifts.

- Assuming a modified NFW profile, a stellar-to-halo mass function, and a DM profile concentration, we qualitatively explore the predicted shape of the underlying DM halo density profile for our sample. We find that the higher-mass, baryon-dominated systems would need a cored profile to reconcile their low fractions. This core could have been induced by repeated bursts of star formation. In contrast, the low-mass, high f_{DM} systems are consistent with cuspy DM profiles, suggesting adiabatic contraction pulling more DM into the central regions.

- Finally, we find that our elevated f_{gas} and f_{DM} naturally anticipate the population of over-massive black holes found with JWST at high-redshift, when assuming a $M_{\text{BH}} - M_{\text{dyn}}$ relation.

Our study extends, for the first time, measurements of DM fractions to large statistical samples at high redshift, advancing beyond previous analyses focused on ionised-gas kinematics at cosmic noon. Although our inferences rely on several necessary assumptions, they provide a valuable framework for placing spatially resolved measurements of individual systems into a broader population context. Most importantly, this work establishes a foundation for probing DM haloes through high-redshift observations, which is an essential step toward understanding how baryons and dark matter interact and co-evolve during the early stages of galaxy formation.

ACKNOWLEDGEMENTS

We thank Hannah Übler and Andreas Burkert for the insightful discussions. ALD thanks the University of Cambridge Harding Distinguished Postgraduate Scholars Programme and Technology Facilities Council (STFC) Center for Doctoral Training (CDT) in Data intensive science at the University of Cambridge (STFC grant number 2742605) for a PhD studentship. ALD and ST acknowledge support by the Royal Society Research Grant G125142. AJB acknowledges funding from the "FirstGalaxies" Advanced Grant from the European Research Council (ERC) under the European Union's Horizon 2020 research and innovation programme (Grant agreement No.

789056). ECL acknowledges support of an STFC Webb Fellowship (ST/W001438/1). FDE and RM acknowledge support by the Science and Technology Facilities Council (STFC), by the ERC through Advanced Grant 695671 “QUENCH”, and by the UKRI Frontier Research grant RISEandFALL. EE, BDJ, MR, CNAW, and YZ are supported by the JWST/NIRCam contract to the University of Arizona NAS5-02105. DJE is supported as a Simons Investigator and by JWST/NIRCam contract to the University of Arizona, NAS5-02105. Support for program #3215 was provided by NASA through a grant from the Space Telescope Science Institute, which is operated by the Association of Universities for Research in Astronomy, Inc., under NASA contract NAS 5-03127. WM thanks the Science and Technology Facilities Council (STFC) Center for Doctoral Training (CDT) in Data Intensive Science at the University of Cambridge (STFC grant number 2742968) for a PhD studentship. BER acknowledges support from the NIRCam Science Team contract to the University of Arizona, NAS5-02105, and JWST Program 3215.

This work is based on observations made with the NASA/ESA Hubble Space Telescope and NASA/ESA/CSA James Webb Space Telescope. The data were obtained from the Mikulski Archive for Space Telescopes at the Space Telescope Science Institute, which is operated by the Association of Universities for Research in Astronomy, Inc., under NASA contract NAS 5-03127 for *JWST*. These observations are associated with program #1180, 1181, 1210 (JADES), #1895 (FRESCO), # 1963 (JEMS) and #3577 (CONGRESS). Support for program #3577 was provided by NASA through a grant from the Space Telescope Science Institute, which is operated by the Association of Universities for Research in Astronomy, Inc., under NASA contract NAS 5-03127. The authors acknowledge the FRESCO team for developing their observing program with a zero-exclusive-access period. The authors acknowledge use of the lux supercomputer at UC Santa Cruz, funded by NSF MRI grant AST 1828315.

DATA AVAILABILITY

The data underlying this article will be shared on reasonable request to the corresponding author. Fully reduced NIRCam images are publicly available on MAST (<https://archive.stsci.edu/hlsp/jades>), with doi:10.17909/8tdj-8n28, doi:10.17909/z2gwmk31, and doi:10.17909/fsc4-dt61 (Rieke et al. 2023; Eisenstein et al. 2023). The NIRCam grism spectra are publicly available on MAST with doi:10.17909/6rfk-6s81 and doi:10.17909/gdyc-7g80 (Oesch et al. 2023).

REFERENCES

- Allen N., et al., 2025, *A&A*, 698, A30
 Barnabè M., et al., 2012, *MNRAS*, 423, 1073
 Behroozi P. S., Conroy C., Wechsler R. H., 2010, *ApJ*, 717, 379
 Behroozi P., Wechsler R. H., Hearin A. P., Conroy C., 2019, *MNRAS*, 488, 3143
 Bell E. F., de Jong R. S., 2001, *ApJ*, 550, 212
 Blumenthal G. R., Faber S. M., Flores R., Primack J. R., 1986, *ApJ*, 301, 27
 Brammer G. B., van Dokkum P. G., Coppi P., 2008, *ApJ*, 686, 1503
 Burkert A., 1995, *ApJ*, 447, L25
 Burkert A., Silk J., 1997, *ApJ*, 488, L55
 Burkert A., et al., 2010, *ApJ*, 725, 2324
 Calabrese E., Spergel D. N., 2016, *MNRAS*, 460, 4397
 Cappellari M., et al., 2013a, *MNRAS*, 432, 1709
 Cappellari M., et al., 2013b, *MNRAS*, 432, 1862
 Carnall A. C., et al., 2023, *Nature*, 619, 716
 Carniani S., et al., 2024, *A&A*, 685, A99
 Ceverino D., Glover S. C. O., Klessen R. S., 2017, *MNRAS*, 470, 2791
 Chan T. K., Kereš D., Oñorbe J., Hopkins P. F., Muratov A. L., Faucher-Giguère C. A., Quataert E., 2015, *MNRAS*, 454, 2981
 Conroy C., Wechsler R. H., Kravtsov A. V., 2006, *ApJ*, 647, 201
 Cooray A., Sheth R., 2002, *Phys. Rep.*, 372, 1
 Courteau S., 1997, *AJ*, 114, 2402
 Covelo-Paz A., et al., 2025, *A&A*, 694, A178
 Covington M. D., et al., 2010, *ApJ*, 710, 279
 Cresci G., et al., 2009, *ApJ*, 697, 115
 D’Eugenio C., et al., 2021, *A&A*, 653, A32
 D’Eugenio F., et al., 2025, *arXiv e-prints*, p. arXiv:2503.11752
 Danhaive A. L., Tacchella S., 2025, *arXiv e-prints*, p. arXiv:2510.07369
 Danhaive A. L., et al., 2025a, *arXiv e-prints*, p. arXiv:2503.21863
 Danhaive A. L., et al., 2025b, *arXiv e-prints*, p. arXiv:2510.06315
 Dekel A., Burkert A., 2014, *MNRAS*, 438, 1870
 Dutton A. A., Macciò A. V., 2014, *MNRAS*, 441, 3359
 Einasto J., 1965, *Trudy Astrofizicheskogo Instituta Alma-Ata*, 5, 87
 Eisenstein D. J., et al., 2023, *arXiv e-prints*, p. arXiv:2306.02465
 El-Badry K., Wetzel A., Geha M., Hopkins P. F., Kereš D., Chan T. K., Faucher-Giguère C.-A., 2016, *ApJ*, 820, 131
 Faucher-Giguère C.-A., 2018, *MNRAS*, 473, 3717
 Foreman-Mackey D., Hogg D. W., Lang D., Goodman J., 2013, *PASP*, 125, 306
 Freundlich J., et al., 2019, *A&A*, 622, A105
 Furtak L. J., et al., 2024, *Nature*, 628, 57
 Genzel R., et al., 2015, *ApJ*, 800, 20
 Genzel R., et al., 2017, *Nature*, 543, 397
 Genzel R., et al., 2020, *ApJ*, 902, 98
 Giménez-Arteaga C., et al., 2023, *ApJ*, 948, 126
 Girelli G., Pozzetti L., Bolzonella M., Giocoli C., Marulli F., Baldi M., 2020, *A&A*, 634, A135
 Gnedin O. Y., Kravtsov A. V., Klypin A. A., Nagai D., 2004, *ApJ*, 616, 16
 Goodman J., Weare J., 2010, *Communications in Applied Mathematics and Computational Science*, 5, 65
 Greene J. E., et al., 2024, *ApJ*, 964, 39
 Hainline K. N., et al., 2024, *ApJ*, 964, 71
 Harikane Y., et al., 2023, *ApJ*, 959, 39
 Hayward C. C., Hopkins P. F., 2017, *MNRAS*, 465, 1682
 Helton J. M., et al., 2024, *ApJ*, 974, 41
 Hopkins P. F., Kereš D., Oñorbe J., Faucher-Giguère C.-A., Quataert E., Murray N., Bullock J. S., 2014, *MNRAS*, 445, 581
 Hopkins P. F., et al., 2023, *MNRAS*, 525, 2241
 Hu W., Barkana R., Gruzinov A., 2000, *Phys. Rev. Lett.*, 85, 1158
 Ivey L. R., et al., 2025, *arXiv e-prints*, p. arXiv:2507.14936
 Ji X., et al., 2025, *arXiv e-prints*, p. arXiv:2501.13082
 Johnson B. D., Leja J., Conroy C., Speagle J. S., 2021, *ApJS*, 254, 22
 Jones B. L., et al., 2025, *arXiv e-prints*, p. arXiv:2510.07376
 Juodžbalis I., et al., 2024, *Nature*, 636, 594
 Juodžbalis I., et al., 2025a, *arXiv e-prints*, p. arXiv:2504.03551
 Juodžbalis I., et al., 2025b, *arXiv e-prints*, p. arXiv:2508.21748
 Kannan R., et al., 2025, *arXiv e-prints*, p. arXiv:2502.20437
 Kashino D., Lilly S. J., Matthee J., Eilers A.-C., Mackenzie R., Bordoloi R., Simcoe R. A., 2023, *ApJ*, 950, 66
 Kennicutt Robert C. J., 1998, *ARA&A*, 36, 189
 Kennicutt R. C., Evans N. J., 2012, *ARA&A*, 50, 531
 Kohandel M., Pallottini A., Ferrara A., 2025, *arXiv e-prints*, p. arXiv:2505.07935
 Kokorev V., et al., 2023, *ApJ*, 957, L7
 Kormendy J., Ho L. C., 2013, *ARA&A*, 51, 511
 Koudmani S., Henden N. A., Sijacki D., 2021, *MNRAS*, 503, 3568
 Koudmani S., Sijacki D., Smith M. C., 2022, *MNRAS*, 516, 2112
 Kravtsov A. V., Berlind A. A., Wechsler R. H., Klypin A. A., Gottlöber S., Allgood B., Primack J. R., 2004, *ApJ*, 609, 35
 Kravtsov A. V., Vikhlinin A. A., Meshcheryakov A. V., 2018, *Astronomy Letters*, 44, 8
 Lee L. L., et al., 2025, *arXiv e-prints*, p. arXiv:2507.11600
 Leja J., et al., 2019, *ApJ*, 877, 140
 Lelli F., McGaugh S. S., Schombert J. M., 2016, *ApJ*, 816, L14

- Lelli F., Di Teodoro E. M., Fraternali F., Man A. W. S., Zhang Z.-Y., De Breuck C., Davis T. A., Maiolino R., 2021, *Science*, **371**, 713
- Leroy A. K., Walter F., Brinks E., Bigiel F., de Blok W. J. G., Madore B., Thornley M. D., 2008, *AJ*, **136**, 2782
- Li P., McGaugh S. S., Lelli F., Schombert J. M., Pawlowski M. S., 2022, *A&A*, **665**, A143
- Lin X., et al., 2025, *arXiv e-prints*, p. arXiv:2504.08028
- Ma X., et al., 2018, *MNRAS*, **477**, 219
- Madau P., Dickinson M., 2014, *ARA&A*, **52**, A15
- Maiolino R., et al., 2024a, *Nature*, **627**, 59
- Maiolino R., et al., 2024b, *A&A*, **691**, A145
- Maraston C., Pforr J., Renzini A., Daddi E., Dickinson M., Cimatti A., Tonini C., 2010, *MNRAS*, **407**, 830
- Marinoni C., Hudson M. J., 2002, *ApJ*, **569**, 101
- Martinsen T. P. K., Verheijen M. A. W., Westfall K. B., Bershadsky M. A., Andersen D. R., Swaters R. A., 2013, *A&A*, **557**, A131
- Martizzi D., Teyssier R., Moore B., 2013, *MNRAS*, **432**, 1947
- Matthee J., et al., 2024, *ApJ*, **963**, 129
- Mazzolari G., et al., 2024, *arXiv e-prints*, p. arXiv:2404.10811
- McClymont W., et al., 2025a, *arXiv e-prints*, p. arXiv:2503.00106
- McClymont W., et al., 2025b, *arXiv e-prints*, p. arXiv:2503.04894
- McClymont W., et al., 2025c, *arXiv e-prints*, p. arXiv:2506.13852
- McGaugh S. S., 2005, *ApJ*, **632**, 859
- McGaugh S. S., 2012, *AJ*, **143**, 40
- McGaugh S. S., Schombert J. M., Bothun G. D., de Blok W. J. G., 2000, *ApJ*, **533**, L99
- McMillan P. J., 2017, *MNRAS*, **465**, 76
- Milgrom M., 1983, *ApJ*, **270**, 384
- Miller S. H., Bundy K., Sullivan M., Ellis R. S., Treu T., 2011, *ApJ*, **741**, 115
- Moore B., 1994, *Nature*, **370**, 629
- Moster B. P., Somerville R. S., Maulbetsch C., van den Bosch F. C., Macciò A. V., Naab T., Oser L., 2010, *ApJ*, **710**, 903
- Natarajan P., Pacucci F., Ricarte A., Bogdán Á., Goulding A. D., Cappelluti N., 2024, *ApJ*, **960**, L1
- Navarro J. F., Frenk C. S., White S. D. M., 1997, *ApJ*, **490**, 493
- Nelson E. J., et al., 2016, *ApJ*, **828**, 27
- Nelson D., et al., 2019, *MNRAS*, **490**, 3234
- Nestor Shachar A., et al., 2023, *ApJ*, **944**, 78
- Newman S. F., et al., 2013, *ApJ*, **767**, 104
- Noordermeer E., van der Hulst J. M., Sancisi R., Swaters R. S., van Albada T. S., 2007, *MNRAS*, **376**, 1513
- Oesch P. A., et al., 2023, *MNRAS*, **525**, 2864
- Paquereau L., et al., 2025, *arXiv e-prints*, p. arXiv:2501.11674
- Pasha I., Miller T. B., 2023, *The Journal of Open Source Software*, **8**, 5703
- Peacock J. A., Smith R. E., 2000, *MNRAS*, **318**, 1144
- Persic M., Salucci P., Stel F., 1996, *MNRAS*, **281**, 27
- Phillips S., Rizzo F., Kohandel M., Smit R., Pallottini A., 2025, *arXiv e-prints*, p. arXiv:2510.01327
- Pillepich A., et al., 2019, *MNRAS*, **490**, 3196
- Planck Collaboration et al., 2020, *A&A*, **641**, A6
- Pontzen A., Governato F., 2012, *MNRAS*, **421**, 3464
- Pontzen A., Governato F., 2014, *Nature*, **506**, 171
- Pope A., et al., 2023, *ApJ*, **951**, L46
- Price S. H., et al., 2016, *ApJ*, **819**, 80
- Price S. H., et al., 2020, *ApJ*, **894**, 91
- Price S. H., et al., 2022, *A&A*, **665**, A159
- Read J. I., Gilmore G., 2005, *MNRAS*, **356**, 107
- Read J. I., Agertz O., Collins M. L. M., 2016, *MNRAS*, **459**, 2573
- Reines A. E., Volonteri M., 2015, *ApJ*, **813**, 82
- Reyes R., Mandelbaum R., Gunn J. E., Pizagno J., Lackner C. N., 2011, *MNRAS*, **417**, 2347
- Rieke M. J., et al., 2023, *ApJS*, **269**, 16
- Rizzo F., Vegetti S., Powell D., Fraternali F., McKean J. P., Stacey H. R., White S. D. M., 2020, *Nature*, **584**, 201
- Rizzo F., Vegetti S., Fraternali F., Stacey H. R., Powell D., 2021, *MNRAS*, **507**, 3952
- Robertson B., et al., 2024, *ApJ*, **970**, 31
- Rodríguez-Puebla A., Primack J. R., Avila-Reese V., Faber S. M., 2017, *MNRAS*, **470**, 651
- Roman-Oliveira F., Fraternali F., Rizzo F., 2023, *MNRAS*, **521**, 1045
- Rowland L. E., et al., 2024, *MNRAS*, **535**, 2068
- Rubin V. C., Ford Jr. W. K., Thonnard N., 1980, *ApJ*, **238**, 471
- Rubin V. C., Burstein D., Ford Jr. W. K., Thonnard N., 1985, *ApJ*, **289**, 81
- Saintonge A., et al., 2017, *ApJS*, **233**, 22
- Saldana-Lopez A., et al., 2025, *arXiv e-prints*, p. arXiv:2501.17145
- Schneider R., Valiante R., Trinca A., Graziani L., Volonteri M., Maiolino R., 2023, *MNRAS*, **526**, 3250
- Scholtz J., et al., 2025, *A&A*, **697**, A175
- Serra P., Oosterloo T., Cappellari M., den Heijer M., Józsa G. I. G., 2016, *MNRAS*, **460**, 1382
- Sersic J. L., 1968, Atlas de Galaxias Australes
- Shibuya T., Ouchi M., Harikane Y., 2015, *ApJS*, **219**, 15
- Shuntov M., et al., 2022, *A&A*, **664**, A61
- Shuntov M., et al., 2025, *A&A*, **695**, A20
- Sijacki D., Springel V., Di Matteo T., Hernquist L., 2007, *MNRAS*, **380**, 877
- Simmonds C., et al., 2024, *MNRAS*, **535**, 2998
- Simmonds C., et al., 2025, *arXiv e-prints*, p. arXiv:2508.04410
- Simons R. C., et al., 2016, *ApJ*, **830**, 14
- Smith R. E., et al., 2003, *MNRAS*, **341**, 1311
- Sonnenfeld A., Treu T., Gavazzi R., Marshall P. J., Auger M. W., Suyu S. H., Koopmans L. V. E., Bolton A. S., 2012, *ApJ*, **752**, 163
- Speagle J. S., Steinhardt C. L., Capak P. L., Silverman J. D., 2014, *ApJS*, **214**, 15
- Spergel D. N., Steinhardt P. J., 2000, *Phys. Rev. Lett.*, **84**, 3760
- Sun F., et al., 2023, *ApJ*, **953**, 53
- Tacchella S., Dekel A., Carollo C. M., Ceverino D., DeGraf C., Lapiner S., Mandelker N., Primack Joel R., 2016a, *MNRAS*, **457**, 2790
- Tacchella S., Dekel A., Carollo C. M., Ceverino D., DeGraf C., Lapiner S., Mandelker N., Primack J. R., 2016b, *MNRAS*, **458**, 242
- Tacchella S., Bose S., Conroy C., Eisenstein D. J., Johnson B. D., 2018, *ApJ*, **868**, 92
- Tacchella S., Forbes J. C., Caplar N., 2020, *MNRAS*, **497**, 698
- Tacchella S., et al., 2023, *MNRAS*, **522**, 6236
- Tacconi L. J., et al., 2018, *ApJ*, **853**, 179
- Tacconi L. J., Genzel R., Sternberg A., 2020, *ARA&A*, **58**, 157
- Tasitsiomi A., 2007, in *Axebedes M., Fanourakis G., Vergados J., eds, The Identification of Dark Matter*. pp 596–601 (arXiv:astro-ph/0612255), doi:10.1142/9789812770288_0079
- Tiley A. L., et al., 2016, *MNRAS*, **460**, 103
- Trinca A., et al., 2024, *arXiv e-prints*, p. arXiv:2412.14248
- Tully R. B., Fisher J. R., 1977, *A&A*, **54**, 661
- Übler H., et al., 2017, *ApJ*, **842**, 121
- Übler H., et al., 2021, *MNRAS*, **500**, 4597
- Übler H., et al., 2023, *arXiv e-prints*, p. arXiv:2302.06647
- Übler H., et al., 2024, *MNRAS*, **533**, 4287
- Vale A., Ostriker J. P., 2006, *MNRAS*, **371**, 1173
- Wang Y., et al., 2020, *MNRAS*, **491**, 5188
- Ward E., et al., 2024, *ApJ*, **962**, 176
- Wechsler R. H., Tinker J. L., 2018, *ARA&A*, **56**, 435
- Williams C. C., et al., 2023, *ApJS*, **268**, 64
- Wuyts S., et al., 2016, *ApJ*, **831**, 149
- Yang L., et al., 2025, *arXiv e-prints*, p. arXiv:2504.07185
- Zhu Y., et al., 2023, *MNRAS*, **519**, 4479
- de Graaff A., et al., 2024a, *A&A*, **684**, A87
- de Graaff A., Pillepich A., Rix H.-W., 2024b, *ApJ*, **967**, L40
- van Houdt J., et al., 2021, *ApJ*, **923**, 11

APPENDIX A: SUPPLEMENTARY FIGURES

In Figure A1, we present additional diagnostic plots that complement the main analysis. This figure illustrates the relation between the inferred inner DM slope α and the DM fraction f_{DM} , colour-coded by stellar mass and Sérsic index. The trends shown here are

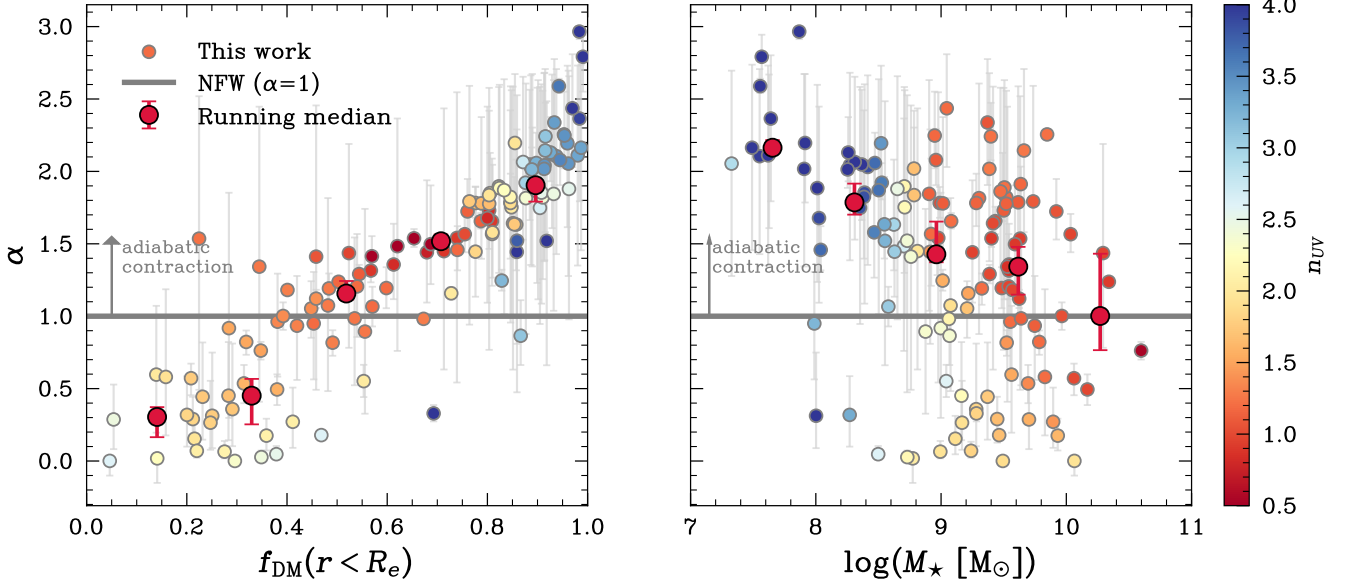


Figure A1. Estimated slope α of the inner DM density profile for a modified NFW distribution (Eq. 18) as a function of measured DM fractions (left) and stellar mass (right). A value of $\alpha = 1$ represents the classical NFW profile, whereas $\alpha < 1$ corresponds to a cored profile, and $\alpha > 1$ to a cuspier profile. We find that galaxies with seemingly steeper DM profiles ($\alpha > 1$) coincide with steeper light distributions ($n > 1$) as probed by the UV stellar continuum. To highlight this, we colour-code the galaxies by the Sérsic index n_{UV} , applying LOESS smoothing (Cappellari et al. 2013b).

consistent with those discussed in Section 5, reinforcing that galaxies with lower f_{DM} tend to exhibit shallower inner density slopes, while systems with higher f_{DM} favour cuspier profiles. Although the scatter is substantial, these correlations support the interpretation that the interplay between baryonic concentration and halo response is already shaping the inner DM structure at $z \sim 5$.

This paper has been typeset from a $\text{\TeX}/\text{\LaTeX}$ file prepared by the author.